

Tensegrity-Blocks: Modular Shape-changing Blocks Enable Self-assembling Robotic Structures

Luyang Zhao^{1*}, Yitao Jiang¹, Muhao Chen², Kostas Bekris³, Devin Balkcom¹

¹Department of Computer Science, Dartmouth College,
Hanover, NH 03755, USA

²Department of Mechanical and Aerospace Engineering, University of Kentucky,
Lexington, KY 40506 USA

³Department of Computer Science, Rutgers University,
New Brunswick, NJ 08901 USA

*To whom correspondence should be addressed; E-mail: luyang.zhao.gr@dartmouth.edu

Modular robots are currently designed to perform a variety of tasks, primarily focusing on locomotion or manipulation through the reconfiguration of rigid modules. However, the potential to integrate multiple functions, such as making each robot deployable and capable of building lattice structures for self-construction and infrastructure creation, remains largely unexplored. To advance the field, we hypothesize that combining tensegrity principles with modular robotics can create lightweight, deformable units capable of integrating three critical functions within a single design: navigating varied terrains, manipulating arbitrary shape objects, and assembling weight-sustainable, active large infrastructures. Here, we designed untethered modular robots that are deformable, lightweight, deployable, outdoor-scale, capable of bearing loads, and capable of 3D attachment and detachment. With these characteristics, the

system can form various 3D structures using different assembly methods, such as walking into position or being transported by rotorcraft. The deformability and lightweight nature of each block enable the assembled structures to dynamically change shape, providing new capabilities such as added compliance during locomotion and manipulation and the ability to interact with the environment in tasks like tent and bridge assemblies. In summary, we suggest that integrating lightweight and deformable properties into modular robot design offers potential improvements in their adaptability and multi-functionality.

Multi-functional blocks that integrate modular design with tensegrity properties for robotic locomotion, manipulation, and structure formation.

INTRODUCTION

Traditional robots are normally highly specialized and effective in controlled environments, designed for specific tasks that require precision, repeatability, and reliability (1). However, in emergency situations, there is a pressing need for robotic systems that are not only versatile but also quickly deployable to address a wide range of challenges. These scenarios often require the rapid assembly of temporary structures, such as antennas, scaffolding, and shelters, as well as the deployment of robots capable of navigating and transporting supplies across unstructured terrain. Drawing inspiration from the capabilities of biological insects, such as army ants (*Eciton* genus), which link their bodies to form bridges across gaps in their foraging paths (2), and fire ants (*Solenopsis invicta*), which form rafts to survive floods (3), researchers have developed modular robots that, though still at the proof-of-concept stage, present several potential advantages. Currently, these robots can adapt to various tasks through reconfiguration and are reusable across different missions, often built with rigid modules with a focus on

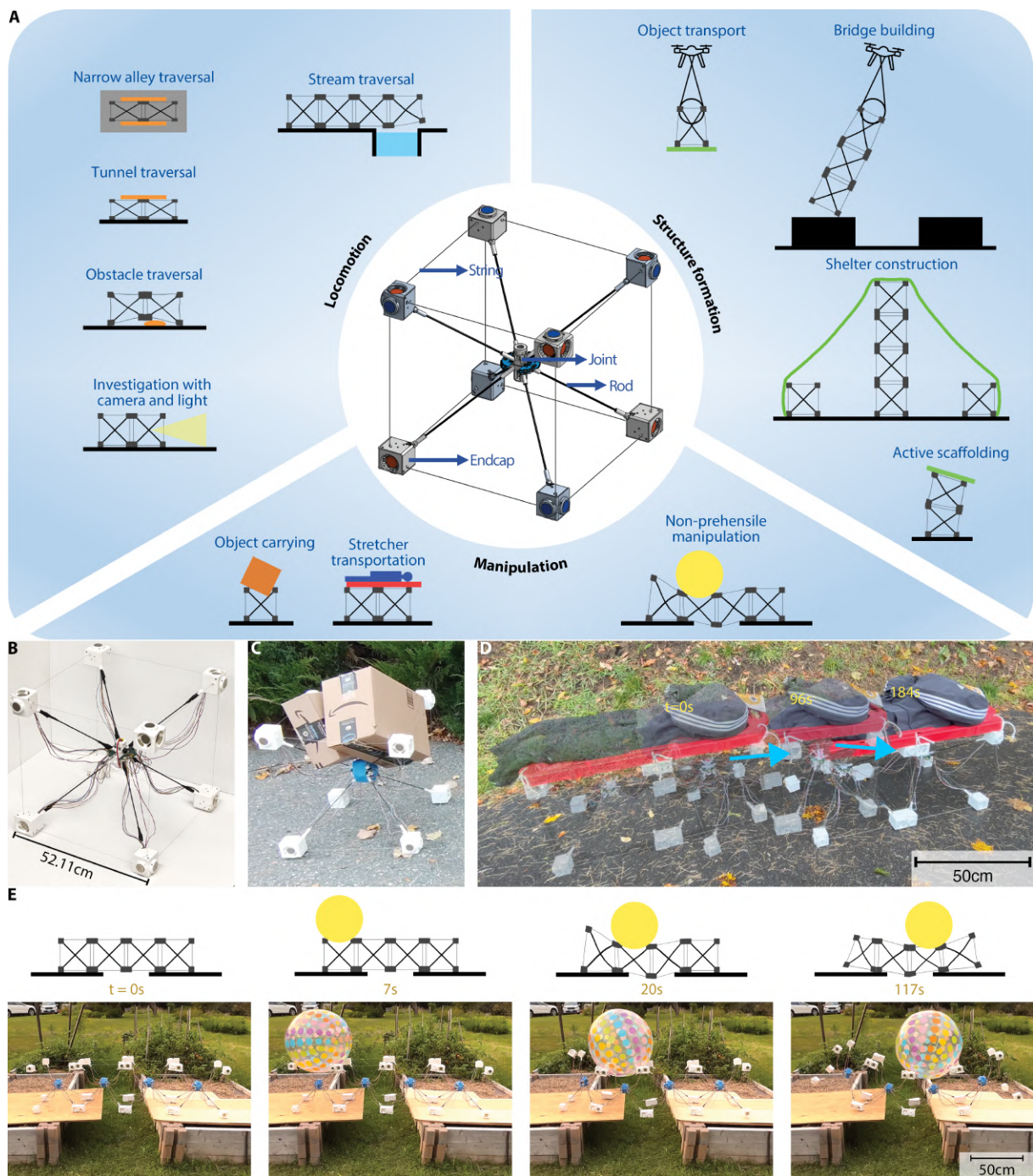


Figure 1: Robot capabilities and examples. (A) System capabilities include locomotion over various terrains and obstacles, manipulation, such as stretcher transportation, as well as structure formation. (B) A single block. (C) Object carrying. (D) Time-lapse transportation of a stretcher mock-up on blacktop. (E) Whole-body wave-like motion transferring a ball.

one or two specific functions, such as locomotion or manipulation (4–6). Recent designs, such as SMORES (7, 8), Sambot (9), showcase how those untethered, self-assembling, rigid modular robots can reconfigure into different configurations to achieve various locomotion patterns. Multi-legged robot swarms (10) successfully incorporated appendages such as limbs into the robot design and showed the capabilities of modular robots to navigate rough outdoor terrains. While modular robotic systems have mainly focused on locomotion (6, 11), there are a few examples of systems that attack manipulation, either using grippers formed from the modules (11), turning a screw with aerial rotorcraft (12), or transporting a table by lifting (13). Despite these advances, a significant gap remains in creating modular robots that are not only adaptable for locomotion and manipulation functions but also easily deployable, packable, and capable of constructing temporary structures on a human scale.

To address this gap, tensegrity structures (14, 15), known for their lightweight design, can sustain significant weight while also being able to deform and adapt to different shapes, making them an ideal complement to modular robotic systems that require both versatility and robustness. They typically consist of rigid components, such as rods, held together by flexible elements like cables or strings, allowing them to be both lightweight and compliant (14). NASA’s Super Ball Bot exemplifies the potential of active tensegrity robots, utilizing cable-driven systems for both landing and locomotion (16). Research studies on pre-assembled tethered module-based tensegrity robots have also demonstrated their effectiveness in outdoor locomotion and as robotic grippers (17, 18), further highlighting the practical applications of these structures. Moreover, the lightweight and deformable properties that are crucial to our design enable efficient transport and deployment via rotorcraft with very limited loading capacities, representing an early but important step toward the development of flexible, rapidly deployable robotic solutions for various applications, including emergency response.

Untethered operation is also crucial for making each module more practical. Small-sized,

shape-changing soft modular robots primarily use three actuation methods. The first is high-current Shape Memory Alloys (SMAs), which allow for quick demonstrations but are difficult to design for untethered use, making outdoor testing challenging (17, 19). Despite this limitation, tethered shape-changing soft modular robots actuated by SMAs excel in manipulation through deformation, whereas rigid robots often need extra parts to achieve similar functionality (6, 20). Pneumatic systems, such as air pumps, also struggle with untethered operation, though Foambot (21) manages untethered vibration using an air pump. A more complex but effective approach is cable-driven systems, which adjust string lengths via motor-pulley mechanisms, offering broader control bandwidth, lower cost, and greater environmental robustness. Eciton Robotica (22) demonstrates untethered operation using this method, showcasing soft modular robots capable of self-assembling. However, fully adaptable, deformable untethered soft modular robots face ongoing challenges such as self-recognition, module communication, and the complexities of assembly and disassembly (11), which need to be addressed for practical deployment in unstructured environments.

Scaling up soft modular robots to human size is beneficial for making them applicable in people-centric and outdoor applications. Some manually assembled modular flexible systems offer meter-scale solutions, such as legged locomotion across various terrains via shape-changing capabilities (23–25). Achieving self-assembly allows for more complex, responsive behaviors, requiring durability in diverse environments and the ability to autonomously navigate and interact with complex terrain. This scale-up also unlocks new possibilities for constructing human-scale infrastructure, such as shelters and bridges. Although the use of active modular robots for human-sized infrastructure construction remains largely unexplored, promising advancements in related fields highlight its potential. For example, passive structures have been successfully assembled using mobile robots and aerial rotorcraft, such as the construction of a 6-meter-tall tower from 1500 foam blocks by quadcopters (26–29). Our work explores the inte-

gration of active modular blocks into rotorcraft-assisted construction, with the goal of enabling the formation of active 3D structures, such as active scaffolding equipped with an antenna that can dynamically adjust to point toward a satellite to increase signal reception.

In this work, we have integrated the properties of modular and tensegrity robots to create a system that embodies five key characteristics essential for each module: (a) lightweight and easily deployable, (b) deformable, (c) untethered operation, (d) designed for outdoor use and capable of bearing loads, and (e) capable of 3D attachment and detachment. With these characteristics, our system can form various 3D structures using different assembly methods, such as walking into position or being transported by rotorcraft. The deformability of each block allows assembled structures to dynamically change shape, while the lightweight nature enables the blocks to be deployable by rotorcraft. These capabilities allow the modules to achieve three distinct functions (Figure 1): (i) effective locomotion across different terrains by adapting their shape, (ii) versatile object manipulation through various methods (grasping and non-prehensile manipulation), and (iii) rotorcraft-assisted assembly into active 3D lattice structures. These functions are not isolated; rather, they interact synergistically, allowing an assembled active structure to potentially perform multiple tasks through whole-body deformation, with the potential to interact adaptively with humans and the environment without requiring reassembly. For example, a snake-like configuration of blocks can move through open spaces, contract to navigate narrow openings, and transport objects along its path. A chain of blocks can form a bridge over a gap by locomotion, with the active bridge also capable of undulating to transport objects across. A human-scale shelter skeleton can lower to facilitate fabric placement and then rise to its full height. These examples showcase the versatility and potential of active structures.

RESULTS

Robot design and characteristics

To meet diverse functional requirements, especially for block deployment and 3D structure formation, we opted for a simple, cubic design for each block, as its symmetrical properties facilitate tiling into larger structures using axis-aligned connectors, reducing the complexity of assembly. Figure 1 illustrates the physical design of a single block, which differs from traditional tensegrity robots like the well-known 3-bar or 6-bar designs where rods are connected solely by strings or cables. Each block in our design features a flexible central joint (TPU printed), which behaves similarly to a ball joint, from which eight rigid rods extend outward in a 3D radial pattern, classifying it as a class-8 tensegrity structure according to *Tensegrity Systems* by Skelton and De Oliveira (14). Each rod terminates in an endcap, with the twelve adjacent pairs of endcaps connected by strings that can be adjusted in length by motors housed within the endcaps. This 3D rotational symmetry across various axes allows for the connection of adjacent blocks in multiple orientations, enabling versatile assembly configurations.

Aiming to achieve untethered operation, all 12 actuators and 12 connectors are integrated into the 8 endcaps, and each block is powered by an onboard Lithium-ion battery capable of supporting locomotion on flat ground for up to 3.5 hours. A customized PCB includes onboard sensing components comprising an Inertial Measurement Unit (IMU), a Wi-Fi module, and an RP2040 microcontroller for twelve-channel encoder processing.

With the focus of creating a lightweight, easily deployable, and outdoor-capable module with a relatively good thumb of load-bearing capacity, we used carbon fiber bars and high-stiffness strings in the design. This choice of carbon fiber enables each module to weigh less than 1.2 kg, with dimensions of 52.11 cm per side length, resulting in a density of 8.53 kg/m³. The blocks are also designed to withstand drops of up to 3 meters onto various outdoor surfaces

without damage (Movie S12), ensuring robustness during rotorcraft-assisted vertical assembly. Each module can support a load of approximately 153.53 N, demonstrating a load-bearing capacity of 13 times its own weight. Additionally, similar to the approach taken for AuxBots (30), we also tested the actuated lifting forces, finding that our blocks can exert forces 7 to 11.5 times their own weight (AuxBots can exert forces 23 to 76 times their weight). Failures typically occur at the carbon-fiber rods. Depending on the specific applications, design adjustments such as using thicker rods or strings may be required for enhanced load-bearing capacity or drop resistance, or employing longer rods for larger-scale module designs.

Flexible central joints and 12 adjustable-length cables (actuated by 12 motors) enable the structure to adapt to various configurations. For instance, shortening four parallel strings while accordingly extending the other eight strings compacts the robot into a flattened shape, reducing its height to 30% (Figure 2(A), Movie S11), while shortening eight strings (extending the other four correspondingly) on two parallel faces compresses it further into a bundle, reducing its volume to 41% of its original size (Figure 2(B), Movie S11). Additionally, four strings on a single face can be shortened to perform a gripping action on external objects. By actuating strings in specific sequences, the robot can also achieve continuous motions to achieve locomotion. To achieve a desired configuration, the controlled string lengths can be determined by solving the nonlinear static equation, $\mathbf{K}\mathbf{n} = \mathbf{f}_{ex} - \mathbf{g}$, using the Lagrangian method described in (31). In this equation, \mathbf{K} represents the stiffness matrix, \mathbf{n} the nodal coordinates, \mathbf{f}_{ex} the external force matrix, and \mathbf{g} the gravitational force matrix. Using the matrix-based form-finding method (32) to solve the static equation allows us to determine all feasible shapes within the robot’s workspace. The workspace for string movements from 0 to l (initial length of the string between two endcaps) and from $0.5l$ to l is depicted in Figure 2(C) and (D), respectively, based on 500 samples. These deformation capabilities allow each robot to not only locomote but also be packed into a compact form for transport and function as a gripper for object manipulation.

To further assess whether the deformation is primarily due to the central joint or if the rods also bend, we conducted experiments measuring the displacement versus force relationship for a single carbon fiber rod, both with and without the central joint. The results show that achieving a 5 cm displacement required approximately 0.5 N with the central joint, compared to 12.8 N for the rod alone (Figure S5). The results indicate that the deformation is primarily due to the central joint, as the rods exhibit significantly higher stiffness and resistance to bending.

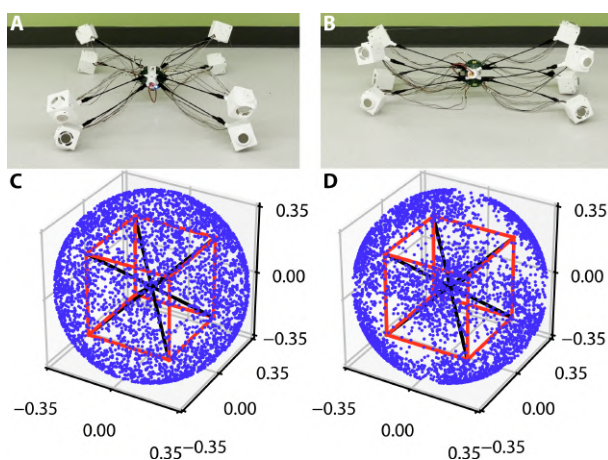


Figure 2: **Two packing strategies and the workspace of a single module subject to different minimum string lengths.** (A) Flattened shape. (B) Bundle shape. (C) Workspace of a single module when min string length equal to 0, (D) and $0.5l$.

For the purpose of enabling robust 3D structure formation, self-assembly, and self-disassembly, we require the connectors between blocks to have four properties: secure connection, error-tolerant attachment, reliable detachment, and power efficiency. Due to the lack of inherent mobility of each individual unit, most existing shape-changing modular robotic systems either depend entirely on manual assembly (23, 33–39) or partially (40–42). In addition, permanent magnets are commonly employed for connection (19, 20, 43), but strong magnets are difficult to separate for detachment. Additionally, the larger the robot, the larger and more impractical the required magnets become. Electromagnets (44) and electro-permanent magnets (45) have been used in rigid modular robots but require heavy coils or substantial electrical

current.

In pursuit of the four desired properties, we designed the connector (Figure 3) with four specific features, each tailored to meet one of our requirements. First, the connector incorporates a mechanically interlocking design that sustains at least 370 N of force per pair of endcaps, ensuring a secure connection that can withstand loads at least 125 times the robot’s weight. Second, permanent magnets are included to mitigate alignment errors, contributing to error-tolerant attachment. Third, the connector allows for reliable detachment through the combination of the first two designs that facilitates easy separation when necessary. Lastly, the connector operates with low power consumption, requiring about 0.06 J of energy per connection via a latch-servo mechanism, and once locked, it does not require additional power to maintain the connection. To evaluate the effectiveness of the magnetic alignment, we conducted experiments by fixing one block’s position and placing another at various angles (0, 15, 30, 45, and 60 degrees) and distances at 1 cm intervals (Figure 4(B)). Our results, shown in Figure 4(D), indicate that at angles of 45 degrees or less, at least one pair of endcaps attaches, enabling further movement toward complete docking. However, at 60 degrees, no attachment is observed. The magnetic force between a pair of endcaps (Figure 4(A(ii)), endcaps a and b) on two modules is shown in Figure 4(C), with the model used for calculation described in the “Supplementary methods” section.

Specific gaits are developed for both the docking and undocking processes. For docking, we designed two specific gaits: *turn_left_fix_vertical_left_front* and *turn_left_fix_vertical_left_back*. Testing these gaits demonstrated that even when only one pair of endcaps initially makes contact, the appropriate gait ensures the successful attachment of the remaining endcap pairs, resulting in 10 successful attachments out of 10 trials. For undocking, an unscrewing motion is employed. This process begins with the shortening of the horizontal strings on the first module and the vertical strings on the second module, followed by reversing the sequence: shortening

the vertical strings on the first module and the horizontal strings on the second module (Figure 4(E), Movie S11)).

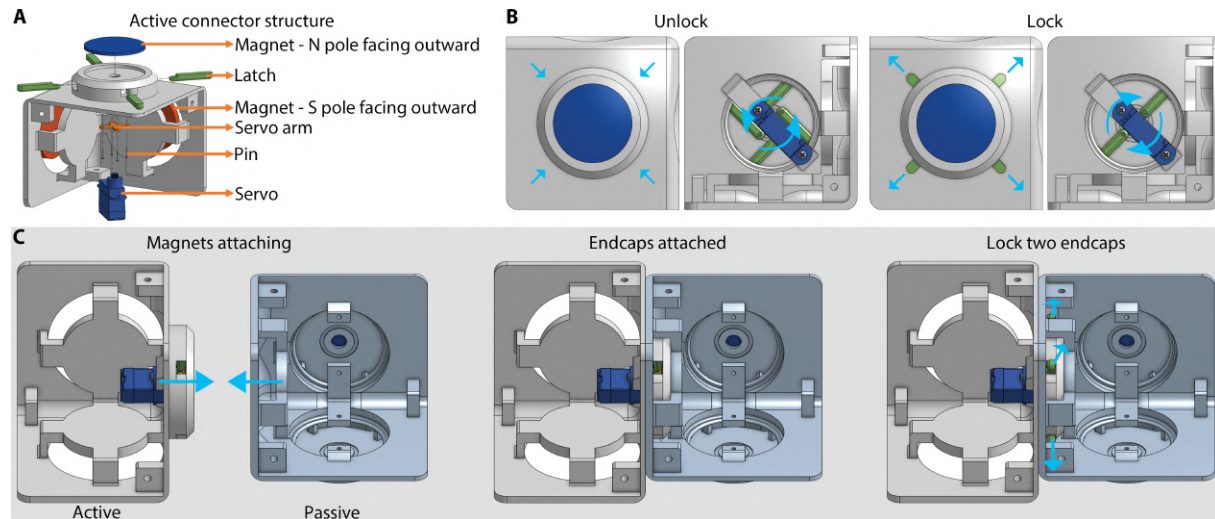


Figure 3: **Endcap design and attachment.** (A) Exploded-view drawing of the active connector. (B) Two states of the active connector: unlocked, with latches rotated inward, and locked, with latches rotated outward. (C) Magnetic alignment to attach and mechanical lock process.

Structure formation

What kinds of active structures can our module design achieve? This section demonstrates several possibilities, including bridges that enable non-prehensile manipulation, tents that expand or contract for use and disassembly, and scaffolding that can rotate to direct an antenna or solar panel.

Rotorcraft plays a key role in the demonstrated deployment, vertical assembly, and providing camera perception. For deployment, the rotorcraft must have a payload capacity exceeding the weight of the module; our modules weigh 1.2 kg, while the DJI Matrice 350 RTK rotorcraft used in this study has a payload capacity of 2.7 kg. The size of the rotorcraft (unfolded, without propellers) is similar to that of one module: 81 cm × 67 cm × 43 cm (L×W×H) compared to 52.1 cm × 52.1 cm × 52.1 cm. We tested the flight duration, which was about 30 minutes,

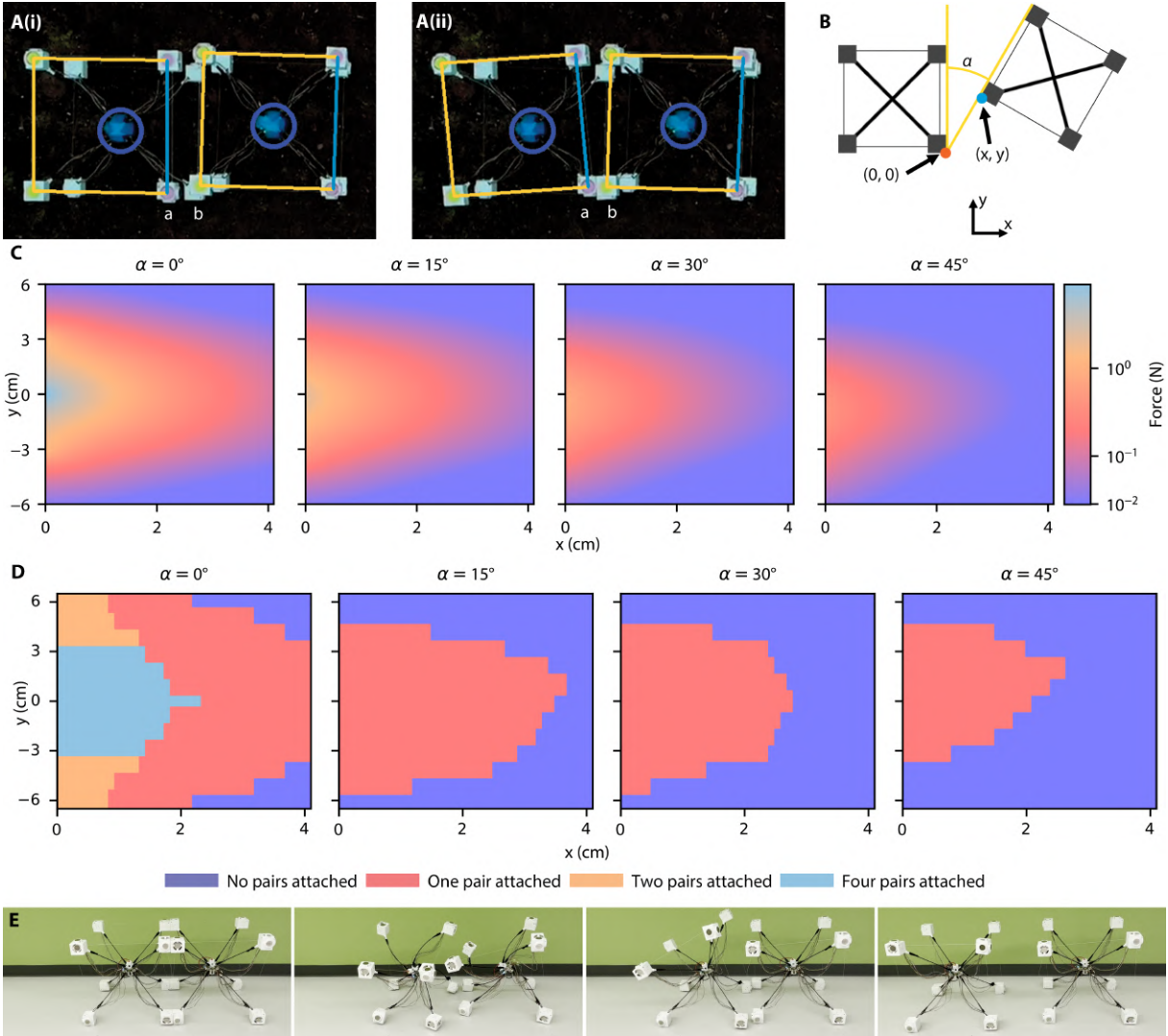


Figure 4: **Attachment and detachment.** (A) State estimation and detection of attachment. (B) Alignment experiment setup for a pair of blocks at different configurations. (C) The magnetic forces between two endcaps at varied distances and angles of 0° , 15° , 30° , and 45° . (D) Alignment robustness contour for a pair of blocks at different configurations. (E) Detachment between two modules.

imposing a constraint on extended assembly tasks.

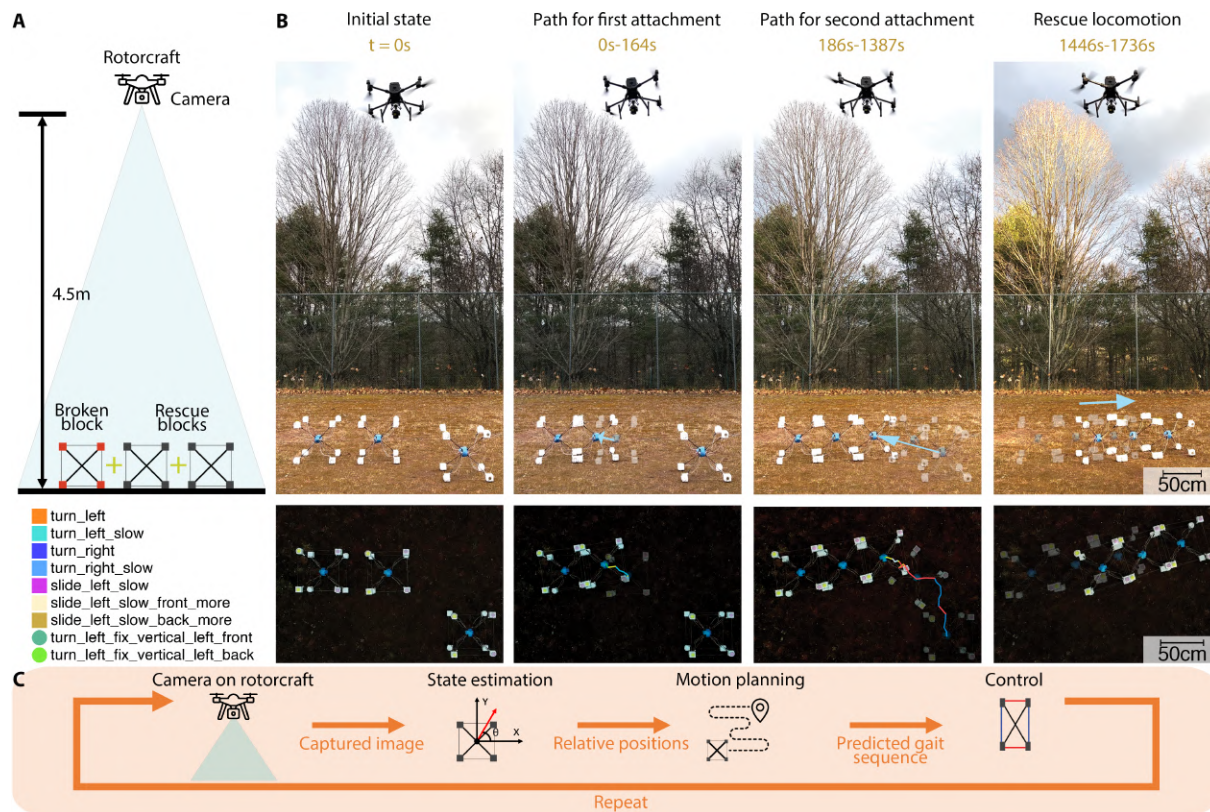


Figure 5: **Planning and control.** (A) A rotorcraft hovers at 4.5 m. Below, three blocks are positioned: one malfunctioning block on the left and two rescue blocks. (B) Side and top views of initial block positions and movement. (C) Operational workflow: on-board control, off-board state estimation, and motion planning.

Terrestrial formation of structures: block connection

The structure formation on land involves attaching pairs of blocks, where one block remains stationary while the other, the active block, selects gaits from predefined gait primitives generated by the *gait generation helper* to approach the target. This attachment process consists of two critical phases: the *approach* phase, guided by real-time motion planning and low-level re-planning to mitigate errors, and the *connection* phase, where blocks are precisely aligned and joined. The transition between these phases is determined by the distance and angular differences between the start and goal positions of the active block. If the start and goal are within

a threshold of 350 pixels (a unit derived from image-based sensing) and 10 degrees, the process advances to the second phase; otherwise, it continues refining the *approach* phase until proximity is achieved.

To ensure accurate real-time sensing during both phases, we employ a rotorcraft-mounted camera to provide a broad field of view and enable rapid repositioning for large modules. Hovering at 4.5 meters, the rotorcraft detects color-coded fiducials—blue for the middle joint and pink/yellow for endcaps—on each block. To estimate the state of each block, we first identify white endcaps via brightness thresholding, establishing boundaries for the colored fiducials. Color detection is then performed within predefined HSV ranges, adjusted for lighting variations. We select $4n$ regions optimized for the desired area-to-perimeter ratio, where n is the number of visible modules. Finally, a global distance minimization algorithm associates each blue joint with its closest color fiducials, allowing precise calculation of each module’s position (x, y) and orientation (θ) . The system operates with a latency of approximately one second, primarily due to image data transmission.

In the *approach* phase, an A* search algorithm is used to find a path to the goal using five selected gait primitives. The modules’ symmetrical design, lacking a defined front, left, right, or back, allows any side to act as the ‘front,’ facilitating directional changes. To reduce the search space, a ‘front’ face is defined based on the color fiducial on each module, with active modules consistently using the left face to connect with passive robots. This simplification, however, comes with a cost— in tight spaces, it may be beneficial to use motions outside this limited set of primitives. Nonetheless, these primitives have been sufficient for the demonstrated examples. We set a maximum of 10,000 iterations for the A* algorithm. If A* fails due to overly tight constraints on reaching the goal, the blocks continue with the gait from the last successful search. If there is no recent path, the blocks use a greedy algorithm to choose the action that most decreases the distance to the goal. The primitives used by A* include *turn_left*, *turn_right*,

turn_slow_left, *turn_slow_right*, and *slide_left_slow*.

In the *connect* phase, the active module employs three sliding mechanisms to make the final approach: *slide_left_slow*, *slide_left_slow_front_more*, and *slide_left_slow_back_more*. When the absolute angular difference between the active and passive modules is large, *slide_left_slow_back_more* is selected if the active module has a larger angular value; otherwise, *slide_left_slow_front_more* is used. When the angular difference is small, the module typically chooses *slide_left_slow*. However, to avoid the possibility of the *slide_left_slow* primitive becoming stuck on a terrain obstacle, there is a small probability that the module randomly selects one of the other two primitives, as shown in the data collected (Figure S2).

To showcase both the system's capabilities in structure formation and its ability to rescue malfunctioning robots, we present an example of a rescue scenario involving a damaged block (see Figure 5 and Movie S1). In this scenario, the far-left block is broken, and the other two blocks act to rescue it. Figure 5(B) shows the side and top views of the blocks, highlighting their automatically planned movement trajectories. The first rescue block attaches to the broken block (0 s - 164 s). Since the malfunctioning block lacks power, only the active connectors on the rescue block are actuated during attachment, resulting in only two pairs of endcaps being connected. The second rescue block then joins (186 s - 1,387 s), and together they pull the broken block to safety (1,446 s - 1,736 s).

Aerial formation of structures: vertical lifting and assembly

To use rotorcraft for vertical assembly, the block grasping mechanism was designed to avoid interfering with the rotorcraft's landing. The mechanism needed to be compliant to handle the challenges posed by wind conditions, which make precise docking difficult. A cable and inflated ball mechanism was developed and attached to the rotorcraft. The rotorcraft positions the ball on top of the block, which then grasps the ball for secure flight. For terrestrial connections, the

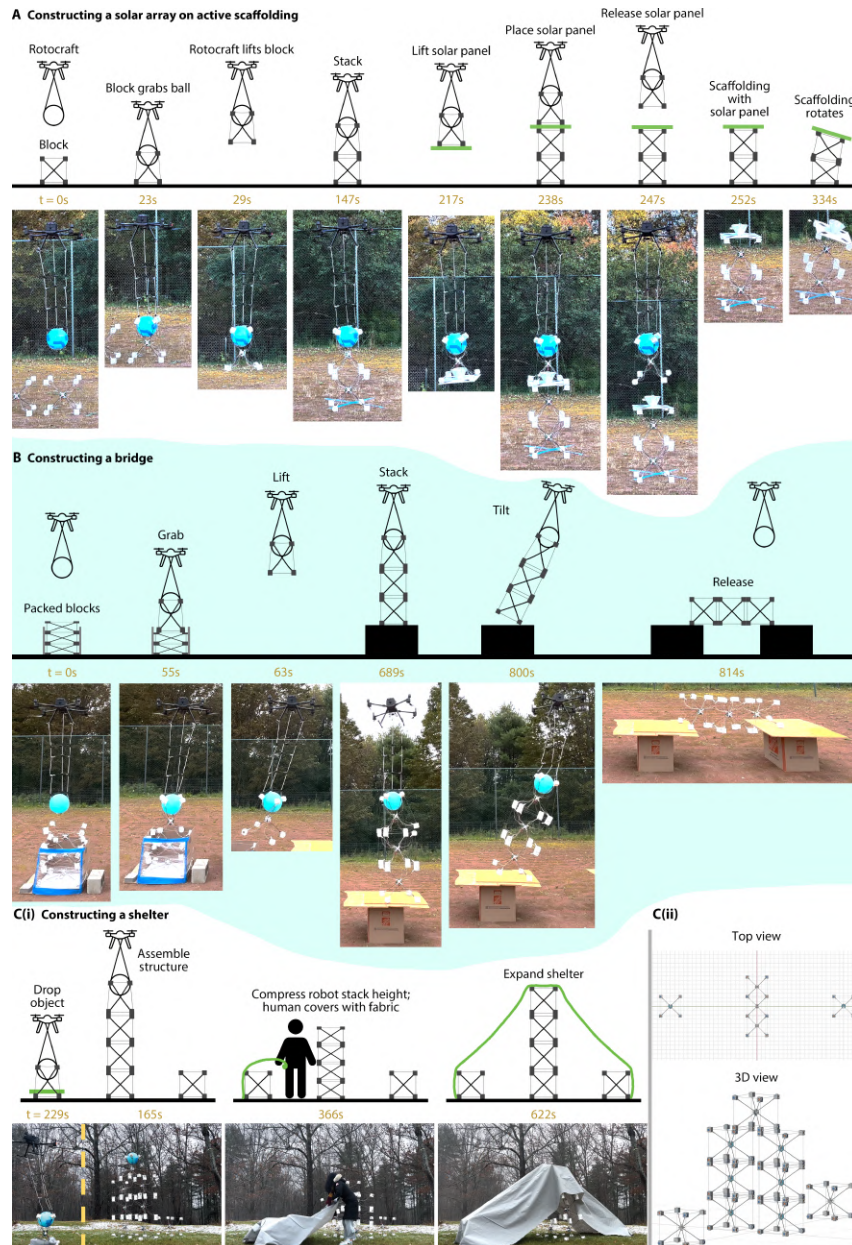


Figure 6: **Structure formation with rotorcraft assistance.** (A) Adaptive scaffolding formation: block-rotorcraft pair transports the block ($t = 23$ s), assembles the structure ($t = 147$ s), and deploys a solar panel ($t = 238$ s - 247 s), with the completed scaffolding rotating up to 360 degrees. (B) Rotorcraft-assisted bridge formation: modules start in a box ($t = 0$ s), the rotorcraft forms blocks into a vertical structure ($t = 63$ s), tilts the structure ($t = 800$ s), and completes a bridge over a 2-block width gap ($t = 814$ s). (C) (i) Rotorcraft aiding in tent skeleton assembly ($t = 165$ s), dropping a block with covering cloth ($t = 229$ s), and tent completion with the stretched skeleton ($t = 366$ s). (ii) Top and 3D views of the block-based tent skeleton.

sensing, planning, and execution loop automates module connections. However, the 1-second latency in the vision system complicates dynamic aerial connections. As a result, the examples in this section were demonstrated using human remote control of the rotorcraft.

Figure 6 shows several examples of how 3D structures, such as tents, adaptive scaffolding, and bridges, can be assembled using a rotorcraft. Figure 6(A) and Movie S4 show a rotorcraft constructing adaptive scaffolding that provides targetable support for solar panels. Once blocks have been assembled into a scaffolding tower, a block then grasps the solar panel and lifts it to position; the tower can then deform to track the sun. Figure 6(B) and Movie S5 show an example of forming a bridge. First, blocks are assembled into a vertical stack on one island; the rotorcraft then tilts the stack to form the bridge. Figure 6(C) and Movie S3 show the construction of a shelter from nine blocks on fairly level grass. The rotorcraft assembles a 2-meter tall structure and delivers the 3 kg fabric. Then, the shelter compresses to be short enough (about 70%) that a human can attach the fabric.

To evaluate the structural stability under varying loads, we analyzed the critical buckling load, which is defined as the load at which a structure is susceptible to global buckling. This critical load was determined by solving the generalized eigenvalue problem for the scalar α , as expressed in the following equation: $-(\mathbf{K}_{G2} + \mathbf{K}_E)d\mathbf{n} = \alpha\mathbf{K}_{G1}d\mathbf{n}$, where \mathbf{K}_{G1} and \mathbf{K}_{G2} represent the geometric stiffness matrices due to external loading and prestress, respectively, and \mathbf{K}_E denotes the material stiffness matrix (46). Using this formulation, we computed the critical buckling compressive loads for various structural configurations. As illustrated in Figure S7, a single-unit configuration exhibited a critical buckling load of 179.07 N. For horizontally combined configurations of two, three, and four units, the critical loads were calculated to be 286.06 N, 286.21 N, and 286.06 N, respectively. Horizontal bridge configurations comprising three and four units demonstrated loading capacities of 187.58 N and 295.85 N, respectively. In contrast, vertically combined units exhibited slightly lower critical loads, with values of 176.83 N, 176.24

N, and 175.93 N for two, three, and four units, respectively. Additionally, the critical buckling load for a tent structure was determined to be 202.59 N. Experimental validation for a single unit under compressive load resulted in a measured critical load of 153.53 N, closely approximating the predicted value of 179.07 N. The observed discrepancy can be primarily attributed to imperfections in the structural bars, strings, and 3D-printed joints. Moreover, the eigenvalues of the stiffness matrices for the ten structural configurations are provided in Figure S7.

Manipulation

A primate may grasp a tool tightly to manipulate it (47). A dolphin playing with a ball employs a *whole-body* non-prehensile approach to manipulation (48). Ants perform cooperative transport by synchronizing individual actions with the group's collective force (49). Different arrangements of robotic blocks and tasks motivate the use of each of these strategies. In this way, the developed system provides a platform for exploring different types of manipulation.

A single module is capable of functioning like a gripper (Figure 6). This capability is demonstrated in rotorcraft deployment, where a block acts as a gripper to hold onto a ball mounted on the rotorcraft. Apart from the ball, the module can grip additional robots, boards, fabric, or balls. This also enables autonomous construction of active structures, similar to how prior rotorcraft systems have constructed passive architectural structures (28, 29).

To demonstrate the potential of modular robots for transporting objects, similar to warehouse robots such as those developed by Kiva Systems - Amazon Robotics (50), which transport shelving units, we present the following examples. As illustrated in Figure 1(C), a single block can transport two boxes. Further, Figure 1(D) and Movie S9 show a pair of blocks transporting a manikin on a stretcher. The manikin used, along with the stretcher, weighs approximately 5 kg, which is significantly lighter than an average human. While the current blocks are neither strong enough to carry a human nor fast enough for emergency response, with further fine-tuning to

improve their weight-sustaining capability, they have the potential to be used for transporting heavier objects in the future.

Biological systems use manipulation capabilities to rescue individuals. For example, ants have been observed to engage in complex behaviors to assist and free trapped members of their colony (51). The previously discussed robotic rescue scenario depicted in Figure 5(B) likewise serves as an example of carrying manipulation.

In addition, manipulation in biology is not limited to animals with opposable thumbs – dolphins can play with a ball (48). Similarly, Figure 1(E) and Movie S10 show how blocks can link to form a dynamic, non-prehensile conveyor system, moving a ball (diameter: 72 cm, weight: 430 g) without the need for direct grasping. This is achieved by the synchronized movements of the connected blocks, simulating the wave motion of a surface that propels a ball. To further explore the adaptability and limitations of this conveyor system, with the same control sequence, we extended our testing to three other objects: a cylinder (perimeter: 180 cm, height: 61 cm, weight: 2,050 g), an irregularly shaped bean bag cushion (max perimeter: 280 cm, height: 1 m, weight: 745 g), and a cuboid box (51 cm × 54 cm × 47 cm, weight: 1,712 g) as shown in Movie S10. The success rate we tested was 5/5 for both the ball and cylinder. The cushion's success rate was lower, 4/5, due to its tendency to fall from the middle of the conveyor before reaching its destination, indicating challenges in maintaining stability for objects with shifting centers of gravity. We tried different initial orientations for the box; manipulation was successful for 2 of the 5 configurations we tried. The box's failures were attributed to one of its corners becoming lodged in the face with four strings, showing the limitations of the system's ability to handle objects with sharp edges and rigid structures.

Locomotion

Robotic locomotion uses two primary strategies. Statically stable approaches, used by *e.g.* Honda’s ASIMO (52), maintain constant balance by keeping the center of mass above a well-defined support polygon. Dynamic gaits, utilized by *e.g.* Boston Dynamics robots (53), allow faster motion, such as running or jumping, but require more sophisticated control approaches. In the paper, we focus on statically stable gaits for their simplicity and ease of control. We note, however, that lightweight robots are also well-suited to dynamic motion strategies (54).

Control and planning strategies in the literature vary, from fully pre-programmed sequences, such as Sony’s dancing robots (55), to gaits generated by machine learning methods that autonomously optimize motion for diverse environments (56). As this work focuses on robot design and capabilities, we implement an approach that sits somewhere in between. A human specifies the basic pattern as a time-dependent sequence of constraints (*e.g.*, the left front foot should be lifted at time 2 s and the left back foot at 6 s while maintaining a maximum width profile of 0.37 m) and an automated *gait generation helper* algorithm constructs the control sequence, determining the string lengths needed to satisfy these constraints. In multi-robot setups, the *gait generation helper* treats the connected endcaps between robots as single units to ensure synchronized movement. More details about *gait generation helper* can be found in the “Supplementary Methods” and Figure S3. For single robots, the gait is inspired by the quadrupedal “amble” pattern (57), where feet on the same side are lifted and moved forward sequentially. In multi-robot setups, the *gait generation helper* coordinates synchronized movement by treating connected endcaps between robots as single units, with feet grouped into two sets based on a zigzag pattern of diagonally adjacent feet. The *gait generation helper* algorithm adapts the control lengths to different environmental constraints, ensuring smooth and coordinated movement.

Locomotion dynamic models

To understand how slopes and surface friction impact walking behavior, we developed a dynamic locomotion model that helps explain why these differences occur and predict their effects. This model not only allows us to create a mechanical theory of locomotion but also provides a framework for testing our hypotheses through experiments. The dynamic model is based on the Lagrangian method (31) and is represented by equation $M\ddot{\mathbf{n}} + D\dot{\mathbf{n}} + K\mathbf{n} = \mathbf{f}_{ex} - \mathbf{g}$, where M , \mathbf{n} , K , D , \mathbf{f}_{ex} , and \mathbf{g} are the mass, nodal coordinates, stiffness, damping, external, and gravitational matrices. The external forces \mathbf{f}_{ex} at the contact points can be divided into parallel ($\mathbf{f}_{ex,\parallel}$) and perpendicular ($\mathbf{f}_{ex,\perp}$) components, satisfying: $\mathbf{f}_{ex} = \mathbf{f}_{ex,\parallel} + \mathbf{f}_{ex,\perp}$. To model how the robot interacts with the ground, we treat the ground as a spring-damper system. Assume the i th node is contacting the ground, the $\mathbf{f}_{exi,\perp}$ and $\mathbf{f}_{exi,\parallel}$ can be written as: $\mathbf{f}_{exi,\perp} = (K_G|n_{zi}| + C_G|\dot{n}_{zi}|) \otimes [0 \ 0 \ 1]^T$ and $\mathbf{f}_{exi,\parallel} = \mu|\mathbf{f}_{exi,\perp}|\text{sgn}(\dot{\mathbf{n}}_i - [0 \ 0 \ \dot{n}_{zi}]^T)$, where K_G , C_G , and μ are the stiffness, damping, and friction coefficients of the ground, and $\text{sgn}(\mathbf{v})$ is an operation that takes the direction of the vector \mathbf{v} .

To validate this model, we conducted physical experiments on three different surfaces: wood, a coir vinyl mat, and sandpaper, each at slopes of 0, 5, 10, and 15 degrees. The surfaces are modeled by adjusting only the friction coefficient in the simulator. We estimated these coefficients by tilting each surface until the robot began to slip, resulting in friction values of $\mu_{wood} = 0.354$, $\mu_{coir} = 0.854$, and $\mu_{sand} = 1.412$. This method does not distinguish between kinetic and static friction coefficients. Comparisons of the simulator’s output with real-world tests are shown in Figure 7. The results show that the simulation provides a useful prediction, with the shapes of the curves for the various surfaces for the simulation qualitatively matching the curves from the experiments. The lowest friction surface (wood; red curve) has the shortest walking distances for the robot per gait cycle for all non-zero slopes in both experiment and simulation. Steeper slopes result in shorter walking distances.

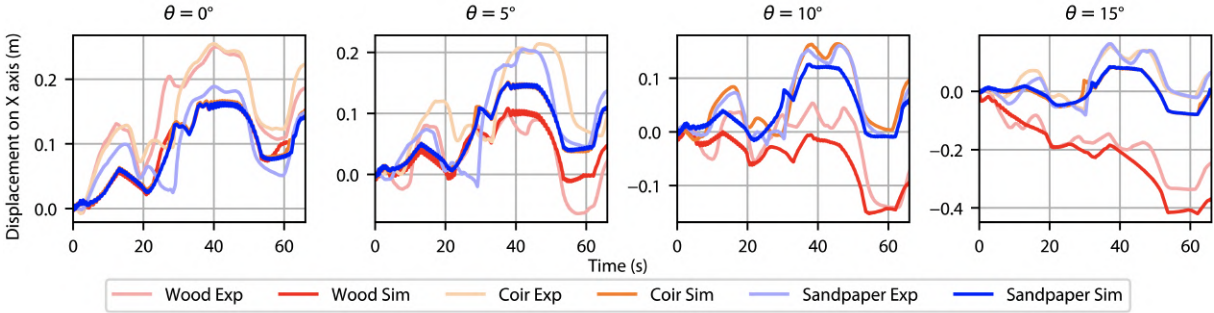


Figure 7: **The historical data for the upper node’s x-coordinate across various surfaces (wood in red, coir vinyl in orange, and sandpaper in blue) and slope angles are presented as follows.** From left to right, slope angles are $\theta = 0^\circ$, $\theta = 5^\circ$, $\theta = 10^\circ$, and $\theta = 15^\circ$, respectively.

Locomotion efficiency and cost of transport

To evaluate the energy efficiency of our locomotion system, we calculated the Cost of Transport (CoT), a dimensionless metric that compares energy efficiency across robotic and biological systems (the details of the calculation can be found in the “Supplementary methods”). The results show that our module is less efficient than some of the aquatic robots, such as octopus-inspired and reconfigurable armed robots (58), but more efficient than a prior motor-driven soft six-bar tensegrity robot (59) and significantly more efficient than soft modular robots actuated by SMAs (20). Specifically, the CoT for single-, two-, and four-module locomotion is 163, 143, and 178, respectively. Further details can be found in Figure S8.

Outdoor locomotion demonstrations

Outdoor environments present unique challenges and opportunities for modular robot locomotion. Depending on how blocks are arranged, different locomotion strategies can be employed to navigate various terrains and obstacles. Figure 8 shows several modes of locomotion: Traversing a stream by lifting the front blocks while walking with the rear blocks on non-level dirt surfaces with leaves and stones (A, Movie S6), traversing a log tunnel (B, Movie S7) and a narrow corridor between trees (C, Movie S8) by changing shape before walking, and a “stan-

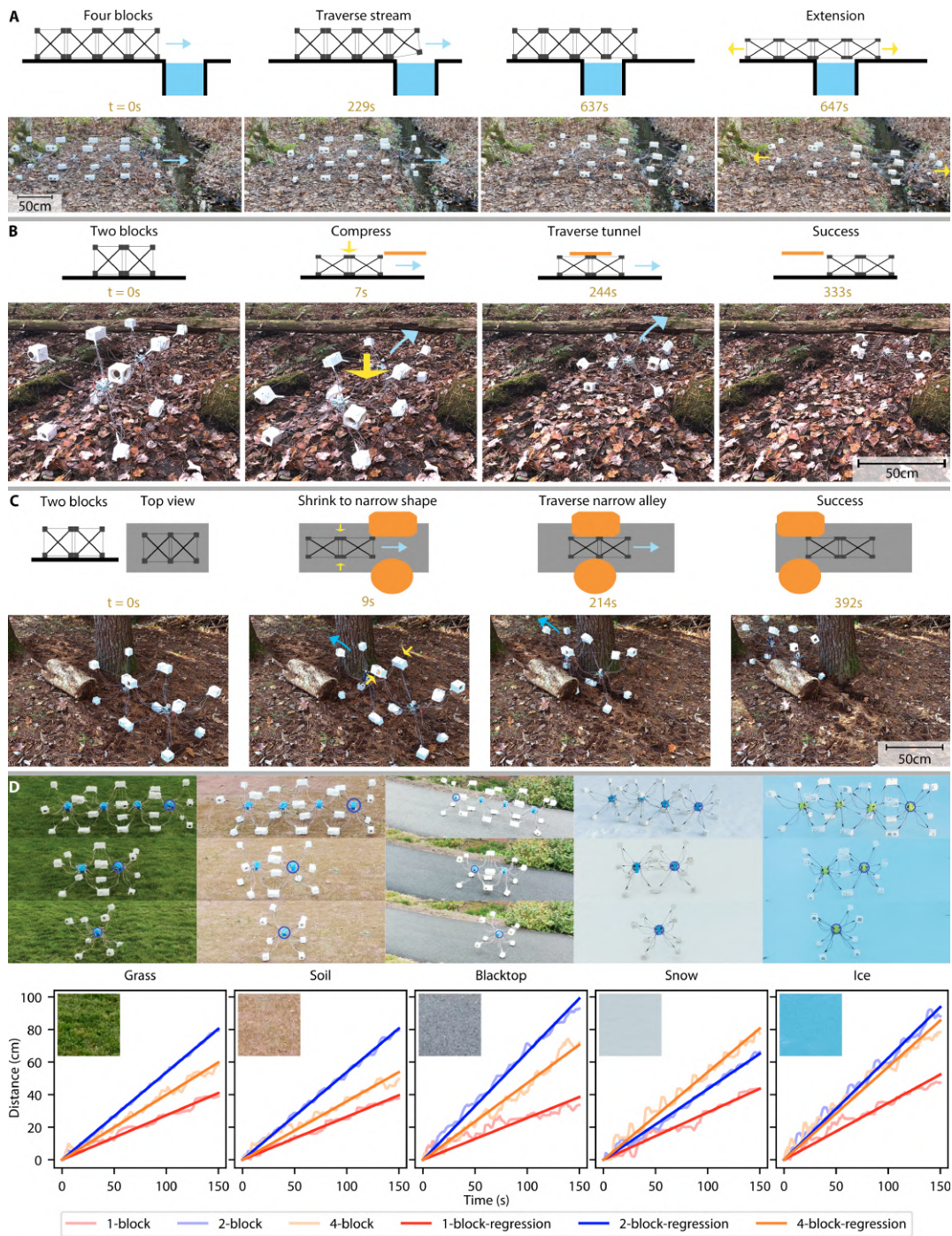


Figure 8: **Locomotion in natural environments.** (A) Four blocks cross a 0.6 m wide stream, indicated by a blue arrow, forming a bridge, shown by a yellow arrow ($t = 647$ s). (B) Two blocks compress vertically to pass under a log tunnel (0.35 m high) from their original height (0.52 m) and then traverse ($t = 244$ s). (C) To navigate a narrow alley (0.37 m wide), the blocks compress horizontally. (D) Speed comparison for different block numbers on grass, soil, blacktop, snow, and ice, with linear regression estimating speeds for each configuration.

ard” locomotion gait (D, Movie S2, Table S2) with speed measurements across grass, soil, asphalt, snow, and ice. For traversing narrow alleys and tunnels, the same gait is employed but with different directional constraints to accommodate the specific environments. In tunnels, the primary constraint is the height (z -coordinate), which must remain below a certain threshold to avoid collisions with the tunnel ceiling. Narrow alleys limit the robot’s maximum width during the gait. From the experimental results, the two-block system is the fastest for all terrains except in the snow scenario, where the four-block system is the fastest. We surmise that the single-block system is slow because only a single foot is lifted at a time, leaving the other three feet down to form a support triangle. For the four-block system, the problem is the opposite – when lifting all diagonal feet in a zigzag pattern, more feet are left on the ground to permit perfect compliance to the surface; some of the “ground” feet are in fact slightly lifted and slip. Different gaits or lower-level control of the compliance of feet to the surface might enable faster locomotion for multi-block systems.

DISCUSSION

Existing modular robot systems have demonstrated the ability to use simple components to achieve a variety of tasks (6, 10). However, they have been primarily limited to locomotion and manipulation tasks (6), lacking the deployability and the capability to build 3D temporary infrastructures. Our study bridges this gap by integrating the principles of tensegrity — characterized by inherent lightweight and deformable properties — into modular blocks, enabling the robots to combine three critical functions within a single design: navigating challenging terrains, performing complex manipulation tasks, and constructing temporary structures with real-world applications.

The mechanical design incorporates eight rods linked by flexible joints and is complemented by active connectors on the endcaps, facilitating 3D structure formation and whole-body defor-

mation, improving manipulation and locomotion in unstructured outdoor environments. Transitioning from indoor to outdoor applications highlighted several environmental challenges, such as fluctuated temperatures affecting battery life and low light conditions impairing state estimation. These issues, coupled with the challenges of navigating diverse terrains like rugged woodland, underscore the need for more robust and adaptive gait optimization strategies for modular systems.

The deployment system, assisted by rotorcraft, enables the rapid assembly of large-scale 3D structures. However, our experiments indicate that further system refinements are needed to handle a larger array of robotic modules and more dynamic tasks. To address these issues, we propose enhancing local processing capabilities on the rotorcraft to reduce latency and improve real-time decision-making, which is vital for dynamic and complex task environments. Moreover, introducing onboard cameras and sensors on the modules themselves could foster a more autonomous and integrated approach to self-assembly, similar to the methods demonstrated by Daudelin et al. (60).

Our research provides a starting point for exploring the use of modular robots in building temporary active structures intended for human use. Inspired by the cooperative behaviors of insect swarms, this study demonstrates the potential of simple, modular units to collaboratively construct functional setups like emergency shelters without complex control systems. The insights from our experiments suggest practical avenues for further development, particularly in enhancing the structural integrity and deployment efficiency of these systems. For instance, a modular-assembled tent structure successfully housed an adult, showcasing its immediate utility. However, other configurations, such as bridges assembled with four modules and stretchers transported by two modules, though effective for specific tasks, currently lack the strength to support human weight. We anticipate that modular shape-changing lightweight blocks will enhance multi-functional robotics, supporting applications such as automated infrastructure con-

struction with integrated structural and actuation elements, compact building blocks for space systems, and deeper insights into biological systems to drive bio-inspired robotics design.

MATERIALS AND METHODS

Block fabrication and design

Each block consists of a flexible central joint, eight magnetic endcaps, and a Printed Circuit Board (PCB). The central joint is a flexible core of the robot, fabricated from Thermoplastic Polyurethane (TPU) material (1.75 mm, Amazon Basics), selected for a combination of flexibility and durability. The central core features an internal cavity sized to house a battery (21,700 3.7 V 4,200 mAh). Carbon-fiber rods (diameter = 3.5 mm; length = 30 cm) were chosen for their high strength-to-weight ratio.

We created two designs for robot endcaps: 2A1P and 1A2P. The 2A1P type comprises two active and one passive connector, whereas the 1A2P type consists of one active and two passive connectors. These endcaps provide structural support for multi-block assemblies and house the motors. Each 2A1P endcap holds two servo motors for locking and unlocking connections and one primary motor for controlling string lengths. For weight balance, the 1A2P type contains one servo motor and two primary motors. The primary motor is an N20 DC motor with a magnetic encoder (12V/30,000 rpm with a 1:298 gear ratio); servo motors are micro 3.7g servo. Two different sizes of magnets are used in the design: for the active connector, a magnet with the N pole facing outward (Amazing Magnets, product number D063J-N42, thickness: 1.59 mm, diameter: 31.75 mm), and for the passive connector, a magnet with the S pole facing outward (Amazing Magnets, product number D125J-N42, thickness: 3.18 mm, diameter: 31.75 mm).

The PCB, detailed in Figure S1, is a six-layer design with a Wi-Fi module, one microcontroller for control commands and sensor data, a second microcontroller for actuation signals, an inertial measurement unit, and temperature sensors.

Experimental design and data analysis

This section presents the experimental design and data analysis approaches utilized to evaluate the performance of robotic modules in locomotion and rotorcraft-based state estimation experiments across different outdoor terrains, employing tracking and computer vision techniques for measurement and analysis.

For the drop test, we tested the block on four different surfaces (Movie S12): hard-packed snow (tensile strength ranging from 0.1 to 1 MPa (61)), grass-covered soil (stiffness from 240 to 1,693 kN/m (62)), hard-packed gravel (stiffness modulus from 126 to 426 MPa (63)), and soil (stiffness from 3 to 22.1 MN/m (64)). To conduct the test, we first used a rotorcraft to grasp the robot from the ground, recording the initial height. The rotorcraft then ascended 3 meters above this height before releasing the robot.

For experiments testing the compressive and tensile properties of a block with a half-meter width, we developed a customized test platform according to standard testing protocols, as shown in Figure S6. In the compression test, a wooden platform was horizontally suspended by strings attached to each corner, which were tension-adjusted to ensure planarity, with a level used to verify horizontality. The load was incrementally increased by filling a centrally-placed bucket with sand (each time 500 g), while a vernier caliper attached to the left T-slots of the support frame measured displacement. A counterweight system was employed to establish an initial load of zero, using a second bucket pre-filled with a calculated amount of sand, connected via a twin-pulley system to balance the weight of the empty bucket and platform. For the tensile test, the module was suspended by a central string that passed through a freely sliding connector within the frame's T-slots to ensure vertical alignment, confirmed with a mounted level. Four equal-length strings were attached to the endcaps on the right face of the module, converging into a single strand that anchored to the right T-slots. Similarly, four strings connected to the left endcaps were merged and routed through a pulley to a bucket, which was gradually filled

with sand to increase the load.

In the alignment experiment (see Figure 4(D)), a paper with grids representing various angles was glued on the ground. We fixed the left block in position and manually positioned the right block to achieve specific initial positions and angles. For each angle, we conducted at least three tests at different positions and used the median value for the final results. Our locomotion experiments were conducted outdoors across a variety of terrains to evaluate the performance of different robotic modules. To quantify the speed of each module on different surfaces, we recorded their movements using a camera system. The robots' central joints were distinctly marked with blue/green tape to facilitate tracking during video analysis.

For accurate distance measurement and speed calculation, we equipped the testing area with boards featuring AprilTags (65) within the camera's field of view. These served as reference points, enabling us to employ computer vision techniques to track the trajectory of the central joints of the blocks. The resulting plots illustrating the distance-time relationship are presented in Figure 8 and Movie S2, where the speed is indicated by the slope of the linear regression. For consistency in multi-block locomotion experiments, we track the first block relative to the direction of movement in all cases.

Rotorcraft-camera state estimation experiments were consistently performed over soil interspersed with small stones, vegetation, or snow. We utilized the DJI Matrice 300 RTK rotorcraft. The rotorcraft was maneuvered to a fixed position at a height of 4.5 m and was equipped with its default camera to capture images at a frequency of 30 Hz. We used a Rybozen 4K audio video capture card to connect the laptop to the remote controller for image transmission. These images with a resolution of $2,560 \times 1,440$ pixels were then utilized for state estimation purposes.

Outdoor structure formation with a rotorcraft includes the construction of bridges, tents, and actuatable scaffolding. An operator manually piloted the rotorcraft using a remote controller. Bridge constructions and actuatable scaffolding were erected over a soil environment, whereas

the tent formation was carried out on grass partially covered with snow.

To classify how each gait affected the displacement and orientation of a block, 25 trials were conducted for each gait to measure the expected results. The resulting net translation and rotation for each trial are illustrated in Figure S2, where 5 outliers for each gait are removed. The mean displacement values among 20 trials for each gait are used for planning.

Supplementary Materials

This PDF file includes:

Methods

Figures S1 to S7

Tables S1 to S2

Other Supplementary Material for this manuscript includes the following:

Movies S1 to S12

References

1. J. F. Engelberger, *Robotics in practice: management and applications of industrial robots* (Springer Science & Business Media, 2012).
2. C. R. Reid, *et al.*, Army ants dynamically adjust living bridges in response to a cost–benefit trade-off, *Proceedings of the National Academy of Sciences* **112**, 15113 (2015).
3. S. Murata, H. Kurokawa, *Self-organizing robots*, vol. 77 (Springer, 2012).
4. L. E. Parker, D. Rus, G. S. Sukhatme, Multiple mobile robot systems, *Springer handbook of robotics* pp. 1335–1384 (2016).
5. M. Yim, *et al.*, Modular Self-Reconfigurable Robot Systems [Grand Challenges of Robotics], *IEEE Robotics Automation Magazine* **14**, 43 (2007).
6. G. Liang, D. Wu, Y. Tu, T. L. Lam, Decoding Modular Reconfigurable Robots: A Survey on Mechanisms and Design, *arXiv preprint arXiv:2310.09743* (2023).
7. C. Liu, M. Whitzer, M. Yim, A Distributed Reconfiguration Planning Algorithm for Modular Robots, *IEEE Robotics and Automation Letters* **4**, 4231 (2019).

8. G. Jing, T. Tosun, M. Yim, H. Kress-Gazit, An End-to-End System for Accomplishing Tasks with Modular Robots, *Proceedings of Robotics: Science and Systems* (2016).
9. H. Wei, Y. Cai, H. Li, D. Li, T. Wang, Sambot: A self-assembly modular robot for swarm robot, *2010 IEEE International Conference on Robotics and Automation* (2010), pp. 66–71.
10. Y. Ozkan-Aydin, D. I. Goldman, Self-reconfigurable multilegged robot swarms collectively accomplish challenging terradynamic tasks, *Science Robotics* **6**, eabf1628 (2021).
11. C. Zhang, P. Zhu, Y. Lin, Z. Jiao, J. Zou, Modular Soft Robotics: Modular Units, Connection Mechanisms, and Applications, *Advanced Intelligent Systems* **2** (2020).
12. J. Sugihara, T. Nishio, K. Nagato, M. Nakao, M. Zhao, Design, Control, and Motion Strategy of TRADY: Tilted-Rotor-Equipped Aerial Robot With Autonomous In-Flight Assembly and Disassembly Ability, *Advanced Intelligent Systems* **5**, 2300191 (2023).
13. Y. Tu, G. Liang, T. L. Lam, FreeSN: A Freeform Strut-node Structured Modular Self-reconfigurable Robot - Design and Implementation, *2022 International Conference on Robotics and Automation (ICRA)* (2022), pp. 4239–4245.
14. R. E. Skelton, M. C. De Oliveira, *Tensegrity Systems*, vol. 1 (Springer, 2009).
15. C. Paul, F. Valero-Cuevas, H. Lipson, Design and control of tensegrity robots for locomotion, *IEEE Transactions on Robotics* **22**, 944 (2006).
16. J. Bruce, *et al.*, SUPERball: Exploring tensegrities for planetary probes, *12th International Symposium on Artificial Intelligence, Robotics and Automation in Space (i-SAIRAS)* (2014).
17. R. Kobayashi, H. Nabae, G. Endo, K. Suzumori, Soft Tensegrity Robot Driven by Thin Artificial Muscles for the Exploration of Unknown Spatial Configurations, *IEEE Robotics and Automation Letters* **7**, 5349 (2022).

18. D. Zappetti, S. Mintchev, J. Shintake, D. Floreano, Bio-inspired tensegrity soft modular robots, *Biomimetic and Biohybrid Systems* (Springer, 2017), pp. 497–508.
19. L. Zhao, *et al.*, StarBlocks: Soft Actuated Self-Connecting Blocks for Building Deformable Lattice Structures, *IEEE Robotics and Automation Letters* **8**, 4521 (2023).
20. L. Zhao, *et al.*, Soft Lattice Modules That Behave Independently and Collectively, *IEEE Robotics and Automation Letters* **7**, 5942 (2022).
21. S. Ceron, M. A. Kimmel, A. Nilles, K. Petersen, Soft Robotic Oscillators With Strain-Based Coordination, *IEEE Robotics and Automation Letters* **6**, 7557 (2021).
22. M. Malley, B. Haghghat, L. Houel, R. Nagpal, Eciton robotica: Design and Algorithms for an Adaptive Self-Assembling Soft Robot Collective, *2020 IEEE International Conference on Robotics and Automation (ICRA)* (2020), pp. 4565–4571.
23. S. Li, *et al.*, Scaling up soft robotics: A meter-scale, modular, and reconfigurable soft robotic system, *Soft Robotics* **9**, 324 (2022).
24. N. S. Usevitch, *et al.*, An untethered isoperimetric soft robot, *Science Robotics* **5**, eaaz0492 (2020).
25. A. Spinos, D. Carroll, T. Kientz, M. Yim, Variable topology truss: Design and analysis, *2017 IEEE/RSJ International Conference on Intelligent Robots and Systems (IROS)* (2017), pp. 2717–2722.
26. J. Werfel, K. Petersen, R. Nagpal, Designing Collective Behavior in a Termite-Inspired Robot Construction Team, *Science* **343**, 754 (2014).
27. C. E. Gregg, *et al.*, Ultralight, strong, and self-reprogrammable mechanical metamaterials, *Science Robotics* **9**, eadi2746 (2024).

28. S. Goessens, C. Mueller, P. Latteur, Feasibility study for drone-based masonry construction of real-scale structures, *Automation in Construction* **94**, 458 (2018).
29. F. Augugliaro, *et al.*, The Flight Assembled Architecture installation: Cooperative construction with flying machines, *IEEE Control Systems Magazine* **34**, 46 (2014).
30. L. Chin, M. Burns, G. Xie, D. Rus, Flipper-Style Locomotion Through Strong Expanding Modular Robots, *IEEE Robotics and Automation Letters* **8**, 528 (2023).
31. S. Ma, M. Chen, R. E. Skelton, Tensegrity system dynamics based on finite element method, *Composite Structures* **280**, 114838 (2022).
32. M. Chen, *et al.*, Energy-efficient cable-actuation strategies of the V-Expander tensegrity structure subjected to five shape changes, *Mechanics Research Communications* **127**, 104026 (2023).
33. S. Mintchev, *et al.*, An underwater reconfigurable robot with bioinspired electric sense, *2012 IEEE International Conference on Robotics and Automation* (2012), pp. 1149–1154.
34. S. Kurumaya, *et al.*, A modular soft robotic wrist for underwater manipulation, *Soft robotics* **5**, 399 (2018).
35. Q. Ze, *et al.*, Soft robotic origami crawler, *Science advances* **8**, eabm7834 (2022).
36. M. A. Robertson, J. Paik, New soft robots really suck: Vacuum-powered systems empower diverse capabilities, *Science Robotics* **2**, eaan6357 (2017).
37. S. W. Kwok, *et al.*, Magnetic assembly of soft robots with hard components, *Advanced Functional Materials* **24**, 2180 (2014).

38. C. D. Onal, D. Rus, A modular approach to soft robots, *2012 4th IEEE RAS EMBS International Conference on Biomedical Robotics and Biomechatronics (BioRob)* (2012), pp. 1038–1045.
39. J.-Y. Lee, W.-B. Kim, W.-Y. Choi, K.-J. Cho, Soft Robotic Blocks: Introducing SoBL, a Fast-Build Modularized Design Block, *IEEE Robotics Automation Magazine* **23**, 30 (2016).
40. S. Ceron, M. A. Kimmel, A. Nilles, K. Petersen, Soft Robotic Oscillators With Strain-Based Coordination, *IEEE Robotics and Automation Letters* **6**, 7557 (2021).
41. A. Vergara, Y.-S. Lau, R.-F. Mendoza-Garcia, J. C. Zagal, Soft modular robotic cubes: Toward replicating morphogenetic movements of the embryo, *PLoS One* **12**, e0169179 (2017).
42. J. Zou, Y. Lin, C. Ji, H. Yang, A reconfigurable omnidirectional soft robot based on caterpillar locomotion, *Soft Robot.* **5**, 164 (2018).
43. J. W. Romanishin, K. Gilpin, D. Rus, M-blocks: Momentum-driven, magnetic modular robots, *2013 IEEE/RSJ International Conference on Intelligent Robots and Systems* (2013), pp. 4288–4295.
44. K. Kotay, D. Rus, M. Vona, C. McGray, The self-reconfiguring robotic molecule, *Proceedings. 1998 IEEE International Conference on Robotics and Automation* (1998), vol. 1, pp. 424–431 vol.1.
45. T. Tosun, J. Davey, C. Liu, M. Yim, Design and characterization of the EP-Face connector, *2016 IEEE/RSJ International Conference on Intelligent Robots and Systems (IROS)* (2016), pp. 45–51.

46. M. S. Khaled, *et al.*, Tensegrity laboratory drilling rig for earth and space drilling, mining, and exploration, *International Journal of Solids and Structures* **252**, 111785 (2022).
47. S. T. Parker, K. R. Gibson, Object manipulation, tool use and sensorimotor intelligence as feeding adaptations in cebus monkeys and great apes, *Journal of Human Evolution* **6**, 623 (1977).
48. F. Delfour, C. Faulkner, T. Carter, Object Manipulation and Play Behaviour in Bottlenose Dolphins (*Tursiops truncatus*) under Human Care, *International Journal of Comparative Psychology* **30** (2017).
49. O. Feinerman, I. Pinkoviezky, A. Gelblum, E. Fonio, N. S. Gov, The physics of cooperative transport in groups of ants, *Nature Physics* **14**, 683 (2018).
50. R. J. F. Barros, J. L. P. Silva Filho, J. V. S. Neto, T. P. Nascimento, An Open-Design Warehouse Mobile Robot, *2020 Latin American Robotics Symposium (LARS), 2020 Brazilian Symposium on Robotics (SBR) and 2020 Workshop on Robotics in Education (WRE)* (2020), pp. 1–6.
51. K. Miler, F. Turza, “O Sister, Where Art Thou?”—A Review on Rescue of Imperiled Individuals in Ants, *Biology* **10** (2021).
52. S. Kim, P. Wensing, Design of Dynamic Legged Robots, *Foundations and Trends in Robotics* **5**, 117 (2017).
53. J. Bhatti, A. R. Plummer, P. Iravani, B. Ding, A survey of dynamic robot legged locomotion, *2015 International Conference on Fluid Power and Mechatronics (FPM)* (2015), pp. 770–775.

54. M. Calisti, G. Picardi, C. Laschi, Fundamentals of soft robot locomotion, *Journal of The Royal Society Interface* **14**, 20170101 (2017).
55. J. Or, Towards the development of emotional dancing humanoid robots, *International Journal of Social Robotics* **1**, 367 (2009).
56. V. Tsonnis, M. Alge, J. Lee, F. Farshidian, M. Hutter, DeepGait: Planning and Control of Quadrupedal Gaits Using Deep Reinforcement Learning, *IEEE Robotics and Automation Letters* **5**, 3699 (2020).
57. B. J. Carr, D. Dycus, Canine gait analysis, *Today's Veterinary Practice* **6**, 93 (2016).
58. C. H. White, G. V. Lauder, H. Bart-Smith, Tunabot Flex: a tuna-inspired robot with body flexibility improves high-performance swimming, *Bioinspiration & Biomimetics* **16**, 026019 (2021).
59. J. Rieffel, J.-B. Mouret, Adaptive and Resilient Soft Tensegrity Robots, *Soft Robotics* **5** (2018).
60. J. Daudelin, *et al.*, An integrated system for perception-driven autonomy with modular robots, *Science Robotics* **3**, eaat4983 (2018).
61. J. Petrovic, Review Mechanical properties of ice and snow, *Journal of Materials Science* **38**, 1 (2003).
62. J. Schramel, C. Peham, Mechanical Properties of a Grass Surface in the Course of a Year, *Equine Veterinary Journal* **48**, 18 (2016).
63. A. Lubis, Z. Muis, T. Iskandar, The study of stiffness modulus values for AC-WC pavement, *IOP Conference Series: Materials Science and Engineering* **309**, 012113 (2018).

64. S. Fiedler, C. Nelson, E. Berkman, A. DiMillio, Soil stiffness gauge for soil compaction control, *Public Roads* **61** (1998).
65. E. Olson, AprilTag: A robust and flexible visual fiducial system, *2011 IEEE International Conference on Robotics and Automation* (2011), pp. 3400–3407.
66. J. D. Head, M. C. Zerner, A Broyden—Fletcher—Goldfarb—Shanno optimization procedure for molecular geometries, *Chemical Physics Letters* **122**, 264 (1985).
67. S. Shuai-Ling, L. Yong-Gang, Z. Yu-Yang, S. Xu-Kun, F. Sheng-Bo, Analysis of magnetic force and potential energy function of multi-stable cantilever beam with two magnets, *Acta Physica Sinica* **69** (2020).

Acknowledgments: We thank R. Kramer-Bottiglio, J. Booth, X. Huang, S. Lu, E. Os-egueda, for helpful discussion; A. Quattrini Li, and M. Jeong for equipment support. **Funding:** Supported by National Science Foundation (NSF): Robust Assembly of Compliant Modular Robots (Award 1954882). **Author contributions:** Conceptualization: LZ, DB, KB; Methodology: LZ, YJ, DB, MC; Investigation: LZ, DB, YJ, KB, MC; Visualization: LZ, YJ, MC; Experiments Design and Implementation: LZ, YJ, DB, MC; System Design and Implementation: LZ, YJ, DB, KB, MC; Algorithm Design and Implementation: LZ, YJ, DB, MC; Funding acquisition: DB, KB; Project administration: DB, LZ; Supervision: DB, KB, MC; Writing: original draft: LZ; Writing: review & editing: LZ, YJ, DB, KB, MC. **Competing interests:** The authors declare that they have no competing interests. **Data and materials availability:** All data needed to evaluate the conclusions in the paper are present in the paper or the Supplementary Materials.

Supplementary Methods

Gait generation helper

The *gait generation helper* works for both single and multi-module setups. In multi-module configurations, the helper considers connected endcaps as one unit and synchronizes the lengths of two strings that connect the same pairs of connected endcaps. The operational workflow of the helper is as follows. *Input*: A sequence of constraints, $\{(P_{C1}, P_{L1}), (P_{C2}, P_{L2}), \dots, (P_{Ci}, P_{Li}), \dots, (P_{Cn}, P_{Ln})\}$, where each (P_{Ci}, P_{Li}) represents constraints configurations and constraints on string lengths at time step i . Some string lengths or configurations may be left unconstrained based on human-designed requirements. The current configuration, modified by the required constraints, is used as the starting point for the optimizer. *Output*: Optimized control sequences $\mathbf{U} = \{U_1, U_2, \dots, U_i, \dots, U_n\}$, where each U_i gives string lengths for a single time step.

The *gait generation helper* iteratively invokes the configuration optimization. The flowchart of configuration optimization is shown in Figure S3; an outer controller optimizes the string lengths to minimize the difference from the desired partial configurations, and the inner simulator calculates the configuration that satisfies the physical constraints as well as string length constraints defined by the outer controller. The Broyden–Fletcher–Goldfarb–Shanno (BFGS) algorithm (66) is utilized for optimization in both the controller and simulator.

Let \mathbf{L} denote string lengths, and let $C(\cdot)$ represent the inner simulator, where the input is the string lengths. The output is the configuration. $P(\mathbf{x}, \mathbf{y})$ takes a full configuration \mathbf{x} and a partial configuration \mathbf{y} as inputs, and extracts elements from \mathbf{x} that are exactly matched in \mathbf{y} . Then, the optimization of the outer controller can be expressed as: $\min_{\mathbf{L}} \sum (P_{Ci} - P(C(\mathbf{L}), P_{Ci}))^2$. The inner simulator calculates the robot's configuration \mathbf{X} that minimizes the elastic potential energy V of the middle joint, which is approximated as the sum of squared differences of

the initial string lengths in cube configuration \mathbf{L}_0 , given the inequality distance constraints \mathbf{L} provided by the outer controller. Let $f(\mathbf{X})$ denote the calculated string lengths based on the configuration \mathbf{X} . The objective function for simulator optimization is $\mathbf{C}(\mathbf{L}) = \underset{\mathbf{X}}{\operatorname{argmin}} V(\mathbf{X}) = \underset{\mathbf{X}}{\operatorname{argmin}} \sum (f(\mathbf{X}) - \mathbf{L}_0)^2$, subject to the inequality constraints: $f(\mathbf{X}) \leq \mathbf{L}$.

For illustrative purposes, consider a representative example detailing a right-turn maneuver. To describe the right turn, a human engineer selects a sequence of requirements for partial configurations and partial string lengths, which are then sent to the *gait generation helper*. Assume the distance between two near endcaps of a module is l . Here is an example input sequence of this locomotion type, using the z heights of various connectors (used as feet) above the ground. (i) The robot starts by elevating its left back foot, with the other three feet remaining on the ground. This configuration is described by $z_1 = 0.5l$, while z_2, z_3 , and z_4 are all zeros. (ii) Following this initial setup, the robot propels its left back foot forward, leading to $z_1 = 0.1l$, $s_{\text{left.bottom}} = 0.3l$, with z_2, z_3 , and z_4 all zeros. (iii) The robot then raises its left front foot, ensuring the remaining three feet retain ground contact. This stage is described by $z_2 = 0.5l$, with z_1, z_3 , and z_4 all zeros. (iv) As a final move, the robot advances its left front foot forward, described by $z_2 = 0.1l$, $s_{\text{left.bottom}} = l$, while z_1, z_3 , and z_4 continue to be zeros. After the engineer generates this sequence, each requirement is used as the input for the configuration optimization to generate the optimized control of the robot, given by the target string lengths. The output string lengths serve as the control commands sent to the blocks.

Modeling of the magnetic forces

To accurately facilitate the connection of modules using the four pairs of magnets, we first analytically model the forces between two magnets at a distance $r(x, y)$ and angle α to quantify the interaction force between them, as shown in Figure 4(B). According to the Biot-Savart Law, the magnetic flux density $d\mathbf{B}$ at position r in 3D-space generated by a filamentary current I in the magnet is given by: $d\mathbf{B} = \frac{\mu_0 I}{4\pi} \frac{d\mathbf{l} \times \mathbf{r}}{r^3}$, where $d\mathbf{l}$ is a vector along the electric currents flow

and μ_0 is the magnetic constant. The magnetic force between two flat cylindrical magnets is calculated by: $\mathbf{F} = \int_{S_1} \int_{S_2} d\mathbf{I} \times d\mathbf{B}$, where S_1 and S_2 are the interacting surface areas of the two magnets (67). In our robot setup, we use two flat cylindrical magnets with the same radius but different magnetic induction values. By varying the distance and angles between two modules, we can determine the magnetic forces between two endcaps (endcaps a and b shown in Figure 4(A)). As seen, the contour in Figure 4(C) shows a good match with the experiment given in Figure 4(D). The color bar denotes the magnetic forces.

Cost of Transport

Cost of Transport is calculated by dividing the energy input into the system by the work done, which can be expressed as: $\text{CoT} = \frac{\int_0^{t_f} P(t)dt + U_0 - U_f}{W_a}$, U_0 and U_f are the total initial and final elastic energy of the structure, and $P(t)$ is the power consumption by the robot with respect to time (in Watts, W), and W_a is the total work done by the active cables at the end of the actuation process: $U_0 = \frac{1}{2}(\mathbf{l}_p - \mathbf{l}_{p0})^T (\hat{\mathbf{E}} \hat{\mathbf{A}} \hat{\mathbf{l}}_{p0}^{-1})(\mathbf{l}_p - \mathbf{l}_{p0})$, $U_f = \frac{1}{2}(\mathbf{l}_p - \mathbf{l}_{pf})^T (\hat{\mathbf{E}} \hat{\mathbf{A}} \hat{\mathbf{l}}_{pf}^{-1})(\mathbf{l}_p - \mathbf{l}_{pf})$, vectors $\mathbf{E} \in \mathbb{R}^{n_e}$ (n_e is the number of elements) and $\mathbf{A} \in \mathbb{R}^{n_e}$ are Young's modulus and cross-section area of all the elements, \mathbf{l}_p and \mathbf{l}_{p0} are the actual length and rest length of all the elements after prestress but before the active actuation strategy. \mathbf{l}_f is the actual final length of all the elements. Notably, smaller efficiency ratios indicate a more efficient cable-actuation process. The work done by the robot depends on the operation. For example, the work done while walking, W_a , can be calculated as $W_a = \mu mgd$, where μ is the coefficient of friction, m is the mass of the robot, g is the gravitational acceleration, and d is the distance traveled by the walking block.

Supplementary Figures

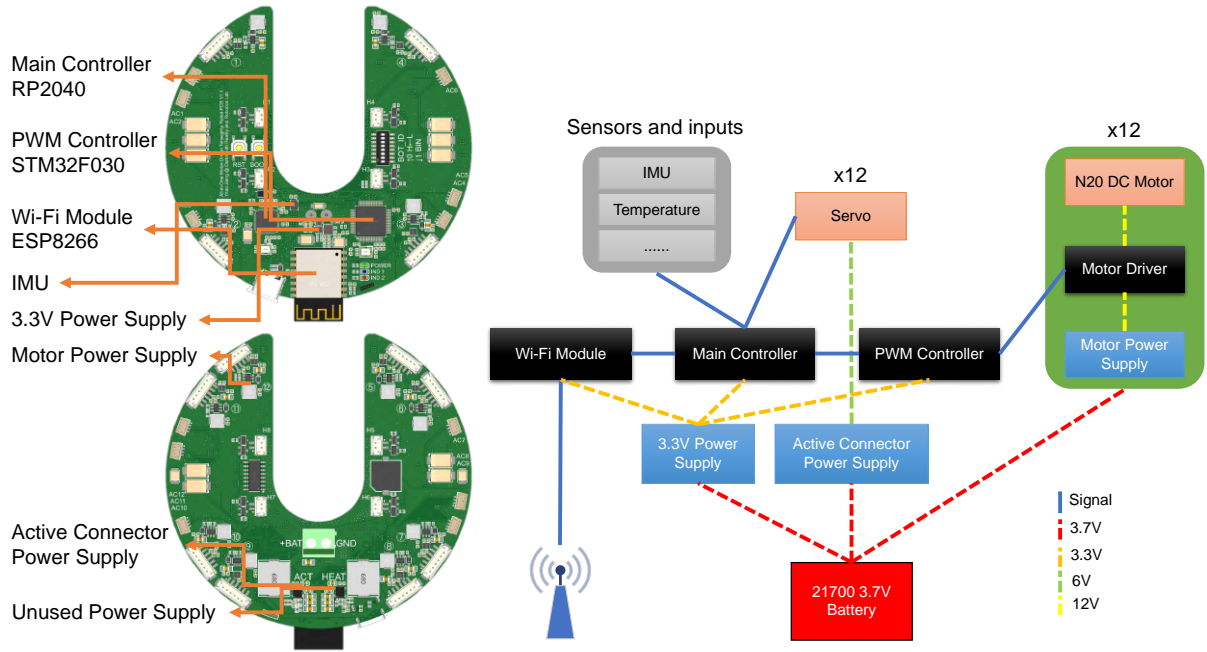


Figure S1: PCB board layout and functional framework of the power delivery and signal transmission.

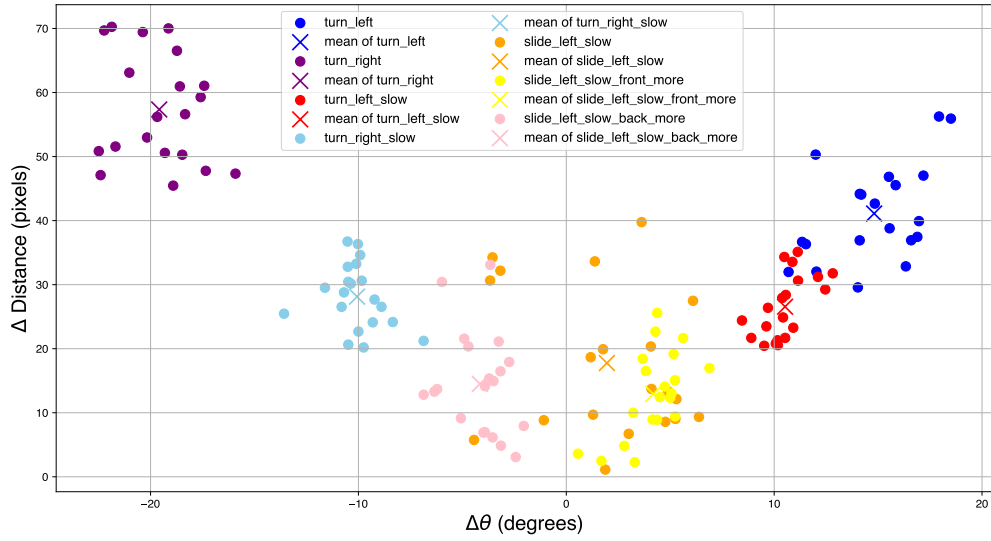


Figure S2: Collected data points for seven different gaits. The displacement and angle differences that each gait can achieve.

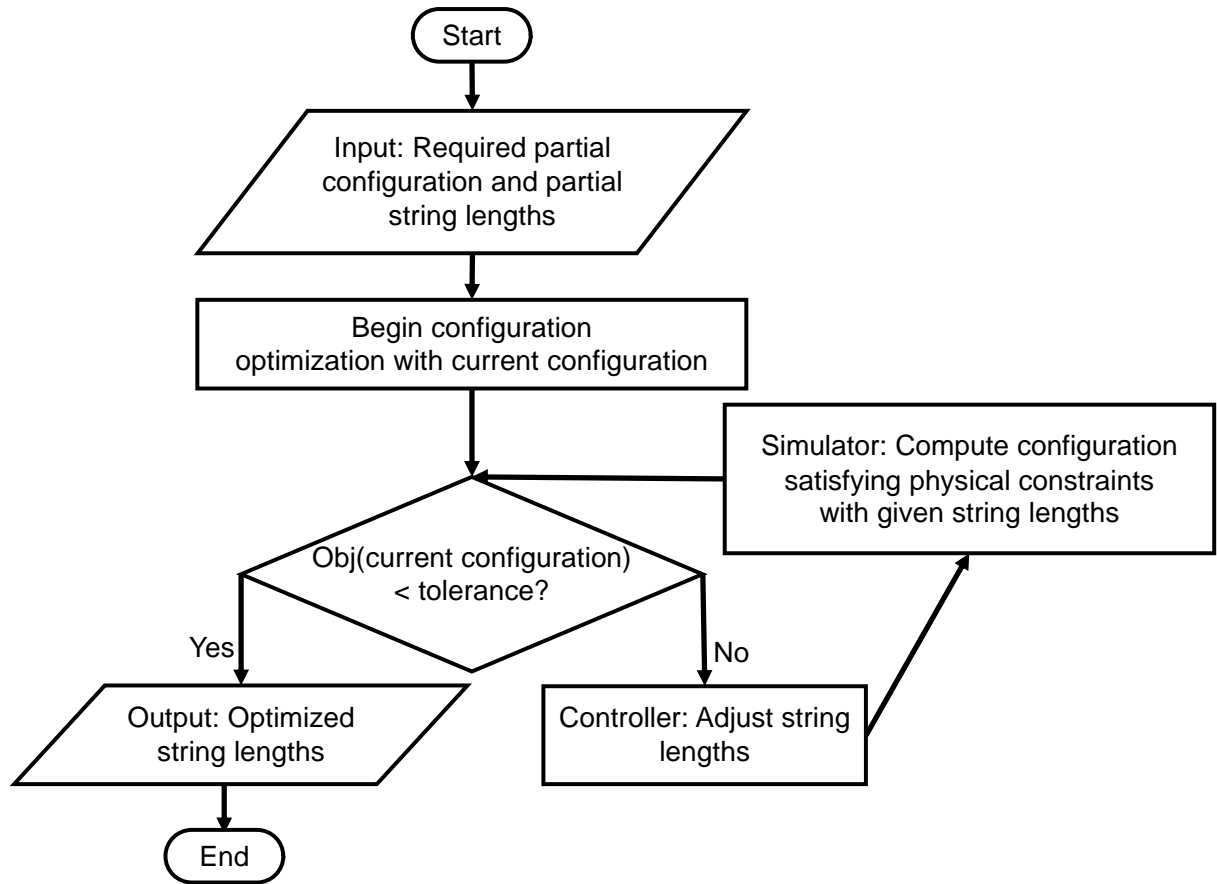


Figure S3: Flow chart of configuration optimization. The process begins with an input generated by an engineer, which is the required partial configuration and string lengths of the blocks. The configuration optimization step checks if the current configuration’s objective value is within the tolerance limit. If not, the controller adjusts all string lengths. These adjusted lengths are then provided as input into a simulator to generate a configuration that satisfies both physical constraints and the given string length inequality constraints. The objective value is reassessed until it falls below the tolerance threshold. Once this condition is met, the optimized string lengths are outputted.



Figure S4: 3D reconstruction of real-world environments, generated by Polycam software. Stream: <https://poly.cam/capture/A26AB51B-AE8D-4135-BF28-94FD225D5521>; Narrow Alley: <https://poly.cam/capture/67A7FA8A-37BF-4FAC-809E-428B47BAE1C5>; Tunnel: <https://poly.cam/capture/66B5090B-433E-42BF-B46B-1BA1C57D3887>.

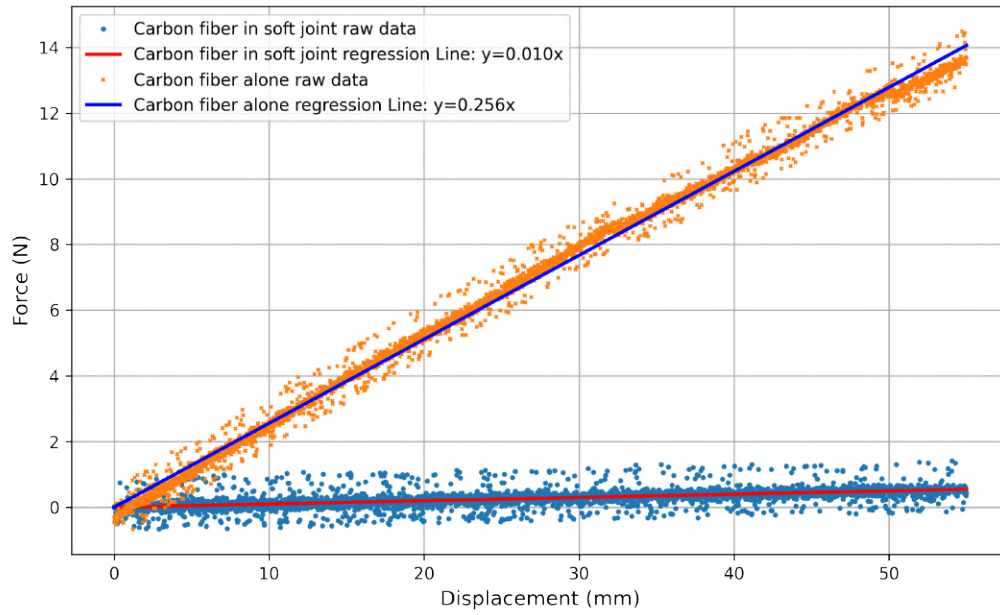


Figure S5: Displacement versus force for a carbon fiber rod in two configurations: with and without a middle joint (TPU).

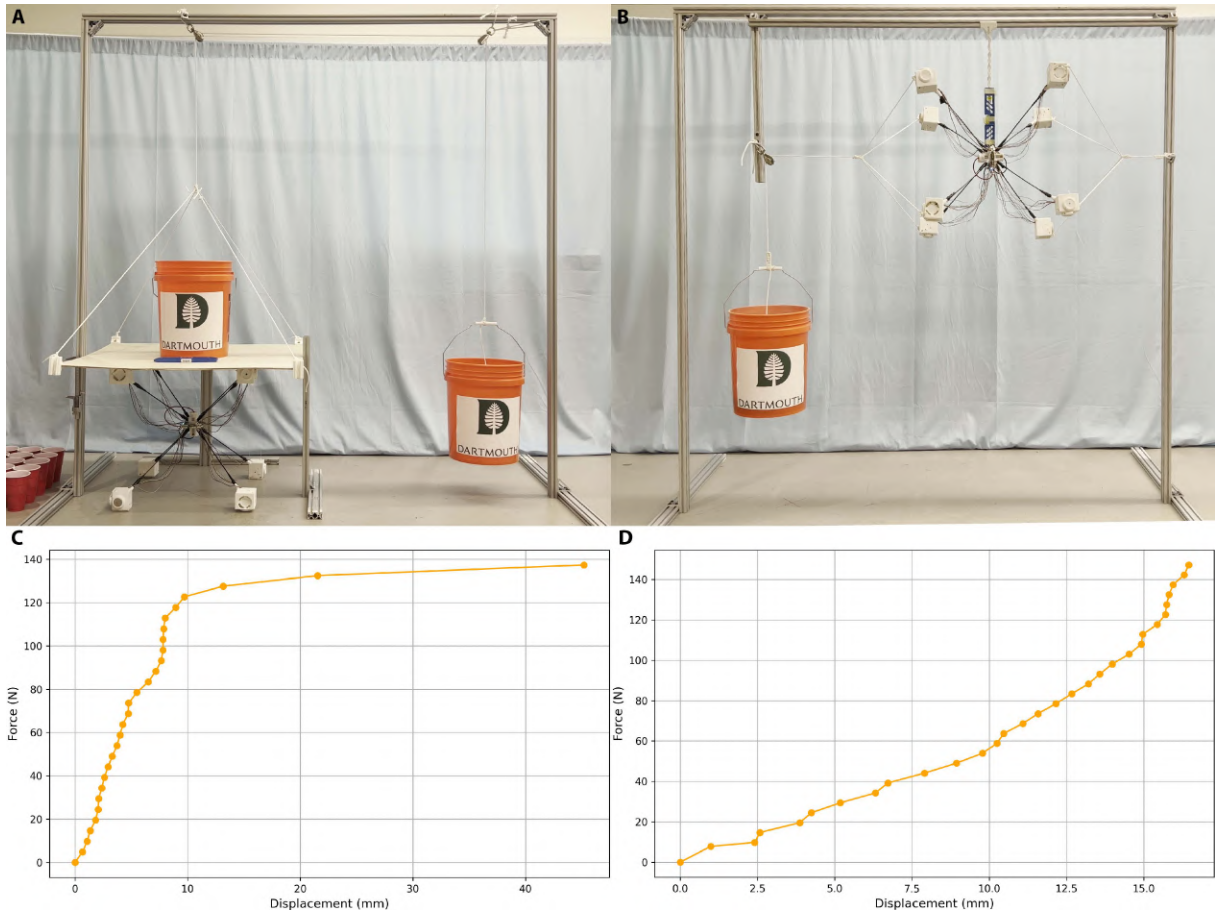


Figure S6: Displacement versus force for a single robot under compression and tension. (A) Compression experiment setup. (B) Tension experiment setup. (C) Results of displacement versus force subject to compression. (D) Results of displacement versus force under tension. During the tests, we measured 500 g of sand in each cup and then carefully poured the sand into the barrel each time, ensuring that the wooden plate remained parallel to the ground. We recorded the displacement from the vernier caliper each time until the modular robot failed.

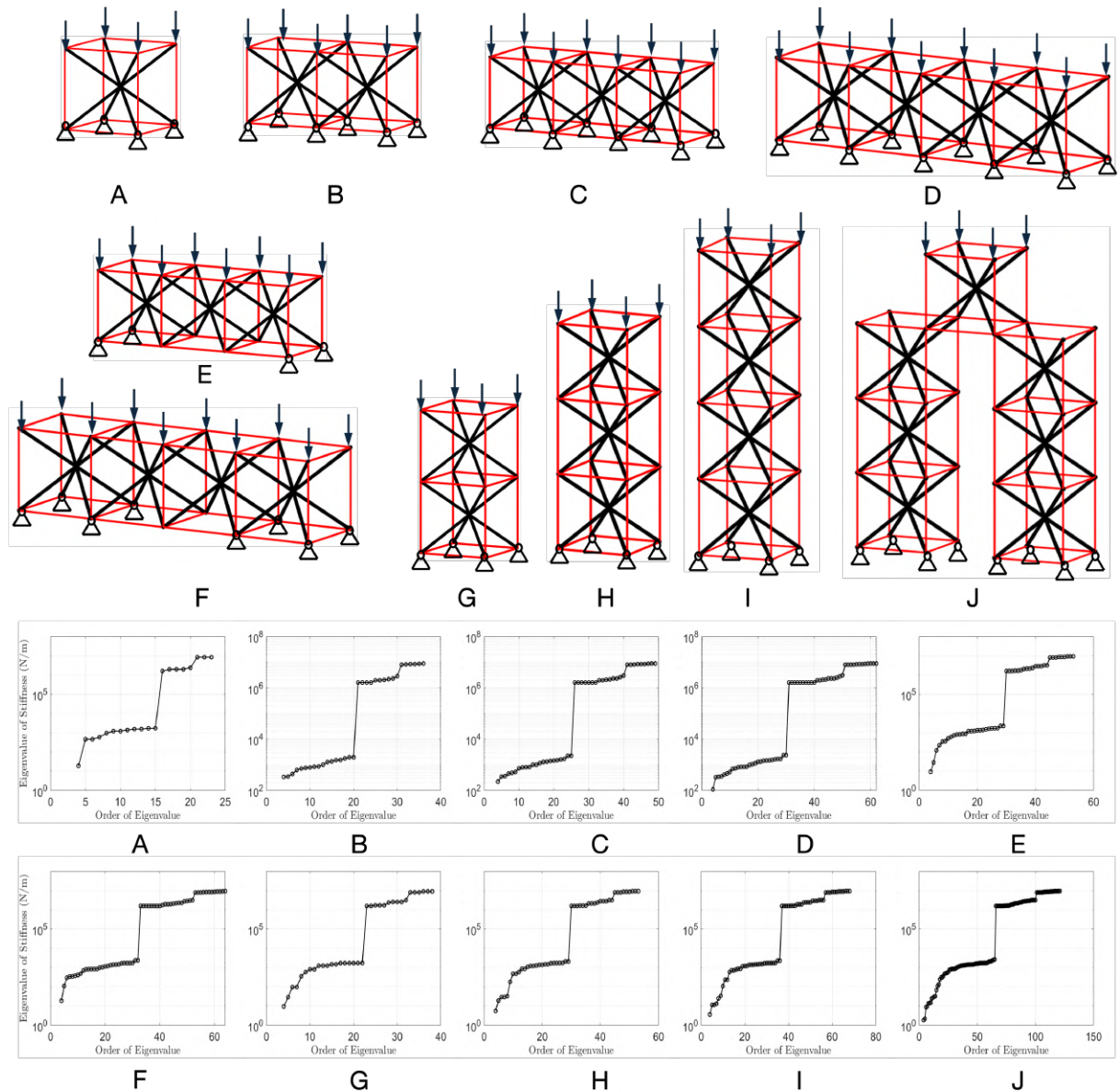


Figure S7: Various structural configurations and stiffness plots. (A) Single unit. **(B)** Two horizontally connected units. **(C)** Three horizontally connected units. **(D)** Four horizontally connected units. **(E)** A bridge: three horizontal units with fewer ground supports. **(F)** A 4-bridge. **(G)** Two vertically stacked units. **(H)** Three vertically stacked units. **(I)** Four vertically stacked units. **(J)** Tent structure.

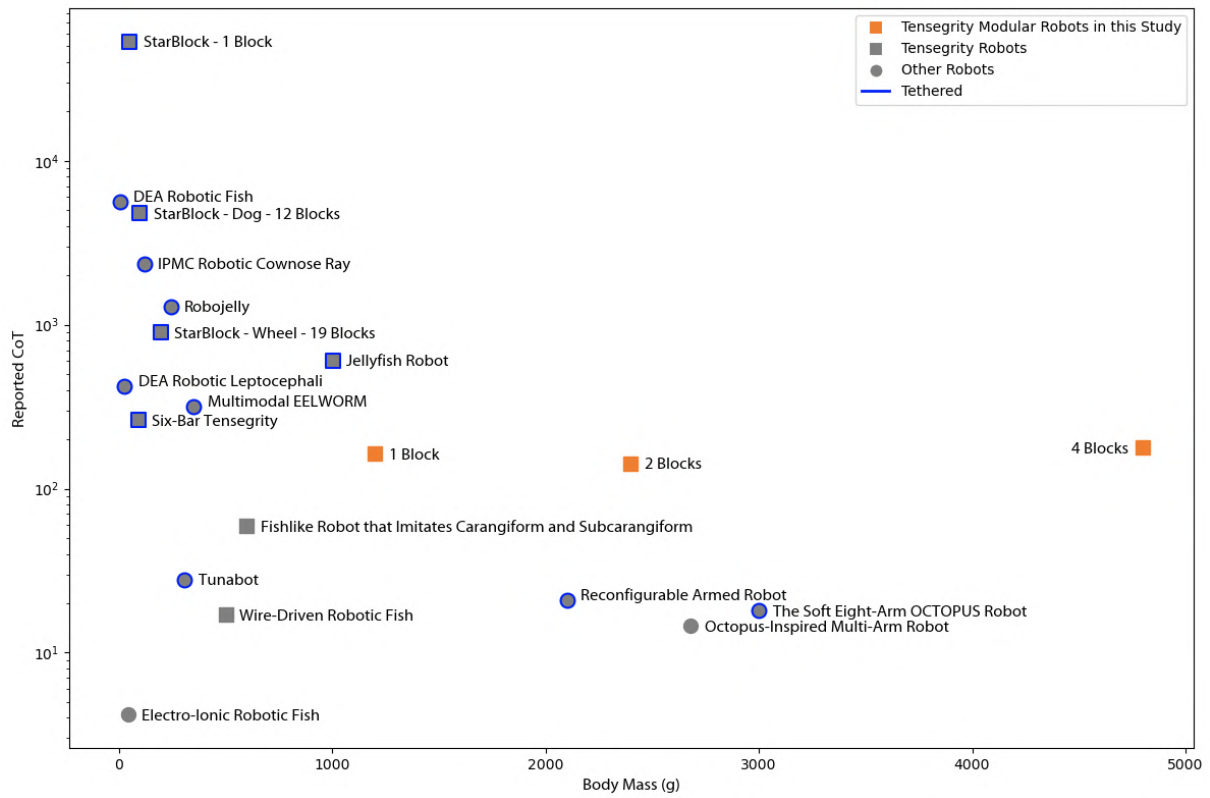


Figure S8: Comparison of our tensegrity modular robots with other robots based on the Cost of Transport (CoT). All referenced data can be found in (20, 58, 59).

Supplementary Tables

Table S1: Comparative analysis of actuation and lifting forces in varied block configurations.

Configuration	Dimensions (cm)	Actuation & Lifting Force
Compressed	58.5×58.5×38	≤ 8.4 kg (≈ 7 robots)
Initial	52.1×52.1×52.1	≤13.3 kg (≈ 11 robots)
Stretched	63×47×47	≤ 13.8 kg (≈ 11.5 robots)

Table S2: Quantitative analysis of module-based locomotion efficacy on various terrains.

Terrain Type	Locomotion Speed (cm/s)		
	1 Module	2 Modules	4 Modules
Grass	0.27	0.54	0.40
Soil	0.26	0.54	0.36
Blacktop (3° slope)	0.26	0.66	0.47
Snow	0.29	0.43	0.54
Ice	0.35	0.63	0.57